Impact of impurity radiation distribution on detachment performance and implications for STEP divertor design

M. Kryjak[1,2], C. Cowley[3], D. Moulton[2], R.T. Osawa[2], S.S. Henderson[2], O. Myatra[2], B. D. Dudson[4], P. Hill[1], L. Pattinson[1], C. Ridgers[1]

[1] York Plasma Institute, University of York, Heslington, York, YO10 5DQ, UK
[2] UK Atomic Energy Authority, Culham Campus, Abingdon, Oxon OX14 3DB, United Kingdom of Great Britain and Northern Ireland
[3] digiLab, Exeter, United Kingdom of Great Britain and Northern Ireland
[4] Lawrence Livermore National Laboratory, Livermore, United States of America

E-mail: mike.kryjak@ukaea.uk

Abstract.

Alternative Divertor Configurations (ADCs) often make use of high total flux expansion (f_R) and connection length ($L_\parallel$) to improve the access to and the controllability of detachment, a regime vitally important for reactor-class tokamaks such as the Spherical Tokamak for Energy Production (STEP). Achieving detachment on such high-power devices is enabled through radiation from seeded impurity species such as argon and neon, which can lead to radiative losses throughout the flux tube, altering the impact of magnetic geometry on detachment. The Detachment Location Sensitivity (DLS) model analytically predicts detachment access and sensitivity based on upstream conditions, the magnetic geometry and seeded impurity radiation. It assumes the radiation region to have no spatial extent. In this work, we relax this assumption and introduce DLS-Extended, a new reduced 1D model which can capture the effects of the spatial distribution of impurity radiation along the field line. The prediction of radiation extent was verified against SOLPS-ITER simulations of an initial STEP design with a good match. DLS-Extended predicts that the radiation extent found in STEP weakens the detachment access benefit of f_R and strengthens the benefit of $L_\parallel$, while the detachment stability of the inner and outer legs is increased and decreased, respectively. This is due to a number of novel radiaton-driven effects and has implications for the optimum strike point position in reactor scale devices. These findings highlight the need for more experimental studies in the presence of broad-radiating impurities. DLS-Extended is distributed under the LGPL-3 open source license and is publicly available on GitHub.

1. Introduction

One of the most pressing issues for reactor-relevant tokamaks is the core-edge compatibility challenge [1] where reactor-scale tokamaks are predicted to produce unmitigated divertor heat loads higher than what known materials can withstand [2, 3]. The most promising solution currently lies in detachment, where the divertor target is protected by the detached region - a cloud of cool neutral gas which reduces direct plasma contact with solid material.

In the detached regime, a high power, high-temperature, conduction-dominated plasma terminates at the interface between the plasma and the neutral region where the majority of power has been dissipated, commonly referred to as the detachment front [4]. Detachment access can be enabled by plasma-neutral interactions, including the reduction of heat flux through radiation, the reduction of momentum through ion-neutral interactions and the reduction of density through recombination [5, 6, 7]. However, in high-power, reactor-class tokamaks, these processes provide insufficient dissipation and require the admission of impurity species such as nitrogen, argon or neon to increase radiative losses [8]. This often leads to impurity radiation dominating the energy losses, a fact used by a class of reduced models based on the Lengyel model [9, 10, 11, 12], including the DLS (Detachment Location Sensitivity) model [13, 4, 14]. The DLS is a simple analytical model able to predict the upstream density, fixed impurity fraction or power required for a given detachment front location using a given magnetic geometry and impurity cooling curve. This allows it to predict detachment access as well as front location sensitivity for a given magnetic geometry, enabling quick scoping studies during early-stage divertor design.

The effects of magnetic geometry on detachment have also been studied across experiments in several devices, including TCV [15, 16, 17, 18], DIII-D [19, 20, 21] and MAST-U [22, 23] as well as in simulations [24, 25, 26], including a comparison of the DLS model itself against SOLPS-ITER slab simulations [4], which found good qualitative, and in some cases, quantitative agreement. While overall, the studies found strong evidence of the benefits of total flux expansion (f_R) and connection length ($L_\parallel$), they found a number of confounding effects such as neutral closure which can make it challenging to isolate the effect of magnetic geometry. The existing body of literature on these effects is covered in detail in section 4. While the DLS model omits several aspects of detachment physics by the virtue of it being a reduced model, it can still provide powerful insight into the impact of magnetic geometry on detachment - both as a framework for first-principles study and a tool for rapid scoping of divertor designs.

Seeded impurity radiation is a crucial requirement for high power devices to achieve detachment [8]. This includes STEP (Spherical Tokamak for Energy Production), the reactor-class tokamak currently being designed in the United Kingdom [27], which utilises argon seeding. So far, very few experimental and simulation studies explored the impact of magnetic geometry in seeded conditions. While the original DLS model captures the impact of impurity radiation, it assumes it has no spatial extent in order to reduce the solution to an analytical form. This assumption was proven invalid in a recent study comparing DLS to MAST-U simulations with impurity transport [14] which found that the radiation extended throughout the divertor even with nitrogen seeding, an impurity often considered to be "narrow-radiating". This motivates the need to consider the effect of impurity distribution on the DLS model predictions and use its first-principles framework to study the impact on divertor magnetic geometry.

In this work, we relax the infinitely-thin radiation region assumption of the original 0D DLS model (also referred to as "DLS" throughout the paper) and introduce DLS-Extended - a new, fast reduced 1D model which self-consistently solves the spatial profiles of heat flux and impurity radiation. We perform a baseline verification of the impurity distribution against SOLPS-ITER [28] simulations of an initial STEP design [29], finding that the simulations predict a broad impurity radiation profile which is well predicted by DLS-Extended for the chosen SOL ring, provided that the exact cooling curve is used. Using this solution as the baseline, we find that a spatially broad radiation region can lead to significant changes in the benefit of f_R and $L_\parallel$ on detachment access for both the inner and outer divertors, leading to a different optimum strike point position.

This paper is structured as follows. First, we introduce the DLS-Extended model and its equations in section 2, followed by the SOLPS-ITER comparison in section 3. In section 4, we define the concept of the detachment threshold and perform an in-depth literature review of its connection with f_R and $L_\parallel$. Section 5 introduces the concepts of detachment window as well as front location sensitivity. The impact of the radiation distribution on the effect of f_R and $L_\parallel$ is explored in section 6, where the DLS-Extended equations are rearranged into

an integral form allowing the decomposition of the detachment access prediction into four terms (section 6.1). Section 6.2 provides a physical interpretation of the terms as well as their impact on detachment threshold. Finally, their impact on the STEP inner and outer divertor design is revealed in a strike point location parameter scan in section 7.1.

The discussion section is divided into three parts: subsection 8.1 summarises the validation status of the physics discussed in this work, subsection 8.2 gives recommendations for STEP divertor design, and finally, subsection 8.3 features a discussion on the known limitations of DLS-Extended, how these limitations could be overcome, as well as some of the most impactful directions for the future of the code. This is followed by the conclusions in section 9.

There are also four appendices. Appendix A features a description of the DLS-Extended solution algorithm, Appendix B contains more detail on the SOLPS comparison, Appendix C reveals the impact of using power as a control variable instead of density or impurity fraction, and Appendix D features the derivation of the expression separating the different radiation effects in section 6.1.

2. DLS-Extended

The original DLS model was first derived in [13], and then re-derived for a simpler coordinate system omitting the upstream region in [4]. DLS-Extended builds on preliminary work in [30] and avoids the thin radiation region assumption by solving the same equations numerically at very low computational cost. The work was motivated by the results in [14], where DLS was compared to nitrogen seeded SOLPS-ITER simulations of MAST-U with impurity transport. The width of the radiation region was found to span a substantial fraction of the divertor leg length despite nitrogen's relatively narrow radiation curve, breaking the thin front assumption. Reactor-class devices consider broader radiating impurities such as neon and argon [8], which could result in broad radiation despite the high power causing steeper temperature gradients which narrow the radiation region. A similar conclusion was drawn in the work of Reinke et al. [12].

The DLS considers conditions at two points: the upstream end of the flux tube (denoted by u throughout this work) and at the detachment front (denoted by f). The upstream could be either the midplane or the X-point. In DLS-Extended, we start with the energy balance equation cast in its continuous form:

$$B\frac{d}{ds}\left(\frac{q_{\parallel}}{B}\right) = n^2 f_\alpha L_\alpha(T) - Q_{in}, \tag{1}$$

Where B is the total B field, $q_\parallel$ the electron parallel heat flux, n the electron density, f_α the fraction of impurity species α, $L_\alpha(T)$ the cooling function of the impurity species with respect to temperature and Q_{in} the uniform energy source term corresponding to cross-field heat transport between the upstream and the X-point. Throughout this work, the upstream is always defined as the midplane. Q_{in} is calculated from a user input of unmitigated X-point

heat flux $q_{\parallel,X0}$:

$$Q_{in} = \frac{q_{\parallel,X0}}{B_X \int_{s_{\parallel,X}}^{s_{\parallel,u}} \frac{1}{B} ds_\parallel}. \tag{2}$$

The electron density is determined by assuming a constant electron static pressure throughout the field line:

$$n = \frac{n_u T_u}{T}. \tag{3}$$

This allows equation 1 to be rearranged in terms of the temperature along the field line, which becomes the first DLS-Extended equation:

$$B \frac{d}{ds}\left(\frac{q_{||}}{B}\right) = \frac{n_u^2 T_u^2}{T^2} f_\alpha L_\alpha(T) - Q_{in}. \tag{4}$$

The second equation is the temperature along the field line obtained by rearranging the Spitzer-Härm equation for parallel electron heat conduction, which is assumed to dominate the heat flux:

$$\frac{dT}{ds} = \frac{q_\parallel}{\kappa_{e0} T^{5/2}}. \tag{5}$$

Both ODEs are numerically integrated given boundary conditions at the front end (low but non-zero values of temperature and parallel heat flux) in a similar fashion to [12]. The model needs the following inputs:

- A parallel profile of the total B field
- $L_\alpha(T)$, the electron cooling function of impurity α
- κ_{e0}, the Spitzer electron conductivity divided by $T^{5/2}$
- Any two of n_u, f_α or Q_{in}
- The front location

The front location is defined by the chosen boundary conditions at the front location. The original Lengyel work [9] defined the point of detachment where the heat flux reaches 0, which is not feasible to implement as the ODE integrator must start from a positive value, and so is typically set to a small non-zero value. The precise choice of the front definition does not affect the results of this study as long as it is kept constant.

The model outputs are the 1D profiles of electron density, temperature, parallel heat flux and radiated power as well as the value of the chosen output variable (one of n_u, f_α or Q_{in}). Details on the numerical implementation, the solver algorithm and boundary conditions are provided in section Appendix A.

DLS-Extended is publicly available on GitHub [31] under the LGPL-3 open source license. The repository includes example Jupyter notebooks which also serve as continuous integration tests.

3. SOLPS-ITER baseline comparison

In order to verify the DLS-Extended predictions of radiation distribution, the results were compared to SOLPS-ITER simulations of an initial STEP design iteration published in [29] featuring midplane fuelling puffs (see Appendix B). The simulated conditions feature a core power flux P_{sep} of 100 MW in a connected double null configuration. The neutral pump is located on the outer wall of the outer divertor leg, and fuelling is primarily achieved through puffing on the inner and outer midplanes, as well as a core particle flux to mimic pellet fuelling. Argon is admitted through a puff in each of the divertor legs - on the inboard wall in line with the X-point, and on the divertor chamber floor below the outer leg, approximately 1/3 of the poloidal distance from the target (see figure 1 in [29]). The reader is directed to [32] for any detailed descriptions of the STEP reactor concept which are beyond the scope of this paper.

The simulations were performed with SOLPS-ITER version 3.0.8. Impurity transport and currents were both evolved, while drifts were neglected. DLS-Extended is a reduced model and features a number of simplifications compared to SOLPS. Electron pressure is assumed to be conserved along the field line, and advection, cross-field transport, and neutral physics are neglected; This leaves density changing inversely proportionately to temperature, which is driven only by impurity radiation and electron conduction. The impact of conduction flux limiters is also neglected, with κ_{e0} kept constant. While SOLPS solves the transport and radiation of each argon charge state, DLS-Extended includes impurity radiation through the fixed-fraction model, where impurity density is a constant fraction of electron density and the radiation is computed from a "cooling curve", which is a function of temperature and assumes a fixed charge state distribution. This means that DLS-Extended does not account for local variations in impurity density, and the results can be sensitive to the choice of cooling curve.

A baseline DLS-Extended simulation was performed on both the inner and outer divertor. The third SOL ring was chosen in each case to strike a balance between the relevance of the flux tube in determining detachment conditions and model validity: maximising the parallel heat flux and minimising the role of cross-field transport and convective heat transfer (see Appendix B). The power source was chosen such that the total X-point parallel heat flux in SOLPS matches the total parallel heat flux in DLS-Extended (where it is purely due to electron conduction). As DLS-Extended is a Lengyel model, the front definition is defined in terms of heat flux, and this was chosen to be the point at which 95% of the total heat flux has been dissipated and choosing an electron temperature of 0.5eV (a small, non-zero number for numerical reasons). This provided a good qualitative profile match with SOLPS for the same front location (see Appendix B), which is an input to the model. The upstream density was set to be the same as in SOLPS. Two cooling curves were used: an ADAS curve with a fixed $n_e\tau$ calculated using the open-source Python package radas [33], and one extracted from the SOLPS simulation for the chosen SOL ring:

$$L_{Ar}^{SOLPS} = \frac{Q_{rad,Ar}}{n_e^2 f_{Ar}}. \tag{6}$$

The value of $n_e\tau$ in the ADAS curve was chosen to be 5×10^{21}ms m^{-3} and comes from a Lengyel study for ITER in [10]. It represents a plausible choice if no high-fidelity simulations are available, and is used in this work to show the sensitivity to cooling curve selection. No attempt is made to tune an $n_e\tau$ parameter to obtain a match to SOLPS for two reasons: firstly, having SOLPS results to tune to implies the exact curves are available, and secondly, due to the SOLPS curves having features which are impossible to match with a constant $n_e\tau$ assumption. More detail is provided in Appendix B.1.

The second difficult input parameter is the conductivity. While it is possible to "extract" it from SOLPS like for the cooling curve (see [10]), this would include the effect of several mechanisms not present in DLS-Extended, such as the variation of conductivity along the field line due to flux limitation, impurities, convection and neutral loss effects. This makes any calculated conductivity value not physically meaningful in a first-principles model, but makes it a useful tuning parameter. Therefore, instead of choosing a physical value, the comparison is performed with the default DLS-Extended conductivity of $\kappa_{0,e} = 2500\text{Wm}^{-1}\text{eV}^{-7/2}$, and then with a value tuned to obtain a match in radiation distribution. This required a moderate increase for the outer and a large increase for the inner: 3200 $\text{Wm}^{-1}\text{eV}^{-7/2}$ and 4750 $\text{Wm}^{-1}\text{eV}^{-7/2}$, respectively. This is likely driven by convective heat flux (see Appendix B).

The outputs of the model are the profiles of radiation, temperature, and heat flux, as well as the absolute value of the constant impurity fraction required for the front to be at the requested position. As this work focuses on scalings and not absolute predictions, the assessment of the accuracy of the impurity fraction prediction is beyond the scope of the paper; see [10, 11] and especially [34] for detailed studies of the absolute accuracy of Lengyel-based models.

The results of the comparison are shown in fig. 1. The SOLPS simulations predict that the impurity radiation is spread over a large region in both divertors, with the outer featuring approximately 20% of the radiation above the X-point. This result shows that the infinitely thin radiation region assumption is invalid in this case, as it was for nitrogen-seeded MAST-U simulations in [14]. The match for the constant $n_e\tau$ curve is poor, with substantially less upstream radiation in the outer and substantially more upstream radiation in the inner leg. This follows exactly from the differences between the chosen $n_e\tau$ curve and the one in SOLPS (see Appendix B.1). Using the SOLPS curve (orange line in figure 1) significantly improves the match. Most of the remaining disagreement can be attributed to convection and density sources and can be compensated for by changing the electron conductivity. This is analysed in-depth in Appendix B, which features detailed results of three SOL rings in each of the divertor legs. The main conclusions are reproduced below:

- The argon puff at the divertor chamber floor boosts radiation halfway down the leg,

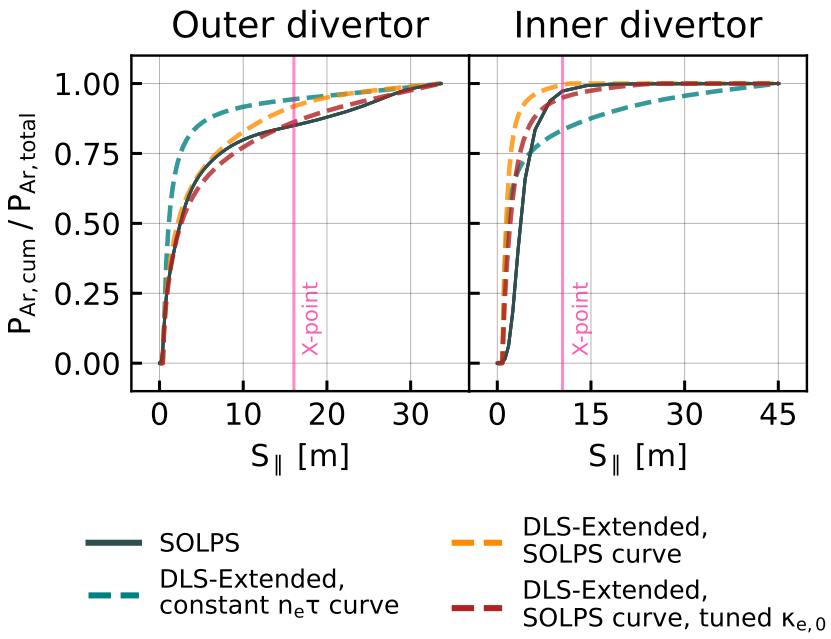

Figure 1: A comparison of the DLS-Extended and SOLPS-ITER radiation distributions for the 3rd SOL ring in the inner and outer divertor shown through a cumulative integral of $P_{rad,ar}$. The x-axis shows parallel distance from target.

dramatically broadening radiation in the SOL rings closest to the separatrix and worsening the match with DLS-Extended. This shows that the impurity radiation distribution can be impacted by puff location (see also [35]).

- The results are sensitive to cooling curve choice, particularly in the high-temperature region which controls upstream radiation. Assuming a constant $n_e\tau$ is insufficient to capture the shape of the effective curve seen in SOLPS, but can give reasonable results if it is close enough.
- Overall, DLS-Extended radiation distribution predictions are reasonable even at high convective fractions, likely due to the temperature profile being driven by conduction.

It can be concluded that DLS-Extended performs well in predicting the parallel extent of impurity radiation for the chosen SOL ring in each divertor, provided that a well-matching cooling curve is used. The remaining disagreement due to convection and sources can be eliminated by tuning electron conductivity. This means that using DLS-Extended without at least some high-fidelity reference simulation will impact the predictions. However, the authors would argue that this is no different to any other application of the fixed impurity fraction approach. In the following sections, only the results with the exact cooling curve and tuned conductivity are used in order to be as representative of the high-fidelity picture as possible.

4. Quantifying influence of magnetic geometry on detachment access

In this section, we provide a detailed breakdown of the known mechanisms behind the impact of total flux expansion and connection length on detachment access, including first-principles effects and ones observed in both experiment and simulation. These are then put in the context of what can be captured by DLS-Extended, before the model is used to reveal additional, novel mechanisms driven by impurity radiation distribution.

First, to establish a framework for quantifying detachment access we follow [13] and define the control variable: a unified detachment actuator combining changes in upstream electron density, impurity fraction of radiating species α and upstream SOL power source:

$$C = \frac{n_u \sqrt{f_\alpha}}{Q_{in}^{5/7}}. \tag{7}$$

Where Q_{in} can be replaced with the unmitigated parallel heat flux at the X-point (as used in [4]) or with P_{SOL} (as used in [13]). The three physical quantities in this actuator are interchangeable in the original DLS, i.e. the change to C can be accomplished by varying any of n_u, $\sqrt{f_\alpha}$ or $Q_{in}^{-5/7}$ completely equivalently. In DLS-Extended, this is still true for n_u and $\sqrt{f_\alpha}$ but only approximately true for $Q_{in}^{-5/7}$, as power variations influence radiation region size through the temperature gradient. Using power leads to a reduction in local detachment sensitivity - see Appendix C.

4.1. Detachment threshold

The control variable at detachment onset is denoted as C_t, with a low value corresponding to easily accessible detachment. Previous DLS literature [13, 4, 14] provides an analytical solution for C and how it is affected by changing two key aspects of magnetic geometry which are the focus of this work: total flux expansion ($f_R = B_X/B_{target}$, the ratio of the total B field at the X-point and at the target) and total parallel connection length ($L_\parallel$). However, in reality a number of additional nonlinear effects exist, including those introduced by DLS-Extended. Therefore, in the present work the geometry effects are framed as a simple proportionality expression, where f_R and $L_\parallel$ affect detachment access according to some proportionality constants $K_{L_\parallel}$ and K_{f_R}:

$$C_t = \left.\frac{n_u \sqrt{f_\alpha}}{Q_{in}^{5/7}}\right|_{threshold} \propto \left[L_\parallel\right]^{-K_{L_\parallel}} \left[f_R\right]^{-K_{f_R}}. \tag{8}$$

In the narrow radiation limit of the original DLS model, $K_{L_\parallel}$ and K_{f_R} reduce to analytically derived values of $K_{f_R} \simeq 1$ and $K_{L_\parallel} = 2/7$. The influence of any additional mechanism manifests as modifications to K_{f_R} and $K_{L_\parallel}$, such as impurity radiation distribution effects which are the focus of the present work.

4.2. Benefit of f_R from first principles

Total flux expansion is defined as $f_R = B_X/B_{target}$, where $B_{target} = B_f$ at the point of detachment threshold. There are two equivalent physical explanations for the f_R benefit. When considering an individual flux tube with both heat flux and radiation on a per unit area basis, f_R increases the cross-sectional area leading to a linearly proportional decrease in heat flux for a constant amount of radiation per unit area. When considering the total divertor plasma volume with a total amount of power to be dissipated, f_R increases the overall plasma volume, leading to a linearly proportional increase in total radiation while the total amount of power remains the same. These are two sides of the same linear proportionality which results in the "classical" scaling of $K_{f_R} \simeq 1$ and is a fundamental principle behind the Super-X divertor design [36, 37]. Since $B \approx B_{toroidal} \propto R^{-1}$, the outer divertor typically features $f_R > 1$ while the inner divertor has $f_R < 1$, i.e. flux compression.

The reason that K_{f_R} is not exactly 1 is due to a minor effect where increasing f_R reduces average B below the X-point, slightly reducing $\int_f^u q_\parallel ds_\parallel$ and therefore T_u, as found [4] as $C_t \propto \frac{B_X^{2/7}}{\langle B \rangle^{2/7}_{above\ \ front}}$. It's a small effect [4] which we lump into K_{f_R} for simplicity.

4.3. Benefit of f_R in literature

The classical scaling of K_{f_R} in the thin radiation limit has been well-reproduced in purpose-designed simulations. A study by Moulton in [24] used minimally-complex SOLPS-ITER simulations without impurity radiation and found $K_{f_R} \simeq 1$ as long as conduction-limited conditions are maintained. An extension of this work by Cowley in [4] using fixed-fraction nitrogen-seeded simulations compared the results to the original DLS model and found a very similar scaling at $K_{f_R} = 1.15$. The simulations featured a narrow nitrogen cooling curve to keep with the thin front assumption.

A similar scaling exists in other simple models which recognised its impact on heat flux in attached conditions, including the modified 2-point model [20], the original DLS model [13] and the recent work by Henderson [32] where the simple model for detachment onset (the "detachment qualifier") from [25] was extended with a term equivalent to $K_{f_R} = 1$ and compared to a database of STEP SOLPS-ITER simulation results. It found good agreement, although the dataset did not span a large f_R parameter space.

A recent unseeded experimental study on MAST-U found that the original DLS model (classical scaling) predictions saw reasonable agreement with experiments comparing a conventional to a Super-X divertor configuration [23], although obtaining a precise, quantitative assessment was constrained by the diagnostics and the impact of f_R was not separated from $L_\parallel$. Experimental validation and modelling studies attempting to isolate the f_R effect paint a complex picture, where competing neutral effects can mask the f_R benefit due to neutral closure changing with strike-point angle, but suggesting that $K_{f_R} \simeq 1$ can be recovered if the divertor is tightly baffled ([20, 15, 38]). Apart from impacting hydrogenic processes, lack of neutral closure can lead to convective cells and high flows in the scrape-off

layer, which reduce K_{f_R} and can even turn it negative in supersonic flows [17].

A recent experimental study in ASDEX [21] found a strong relationship between the total flux expansion and scrape-off layer broadening, which for the initial STEP design considered in the present work would result in the total flux expansion being responsible for λ_{INT} being enhanced by approx. 4 times λ_q. However, the study was performed in a conventional divertor with a small range of outer strike point positions.

In summary, existing studies featuring either narrow, fixed-fraction nitrogen radiation in simulations or even the complete lack of impurity seeding in experiments have generally reproduced the analytical scaling of $K_{f_R} \simeq 1$, which is also confirmed by DLS-Extended in the thin radiation limit. However, there has been insufficient work in seeded conditions, which are found to introduce additional effects in the present work (section 6.2).

4.4. Benefit of $L_\parallel$ from first principles

Total parallel connection length refers to the parallel distance between the midplane and the target. Throughout the whole paper, it is assumed that this is achieved through lengthening L_{div} (the connection length below the X-point) only. We also assume that the length increase is achieved through greater poloidal connection length L_θ, rather than the change in field line pitch angle, unless otherwise specified. The distinction between the two is discussed in section 4.6.

Total parallel connection length impacts detachment through upstream temperature, as can be seen when integrating Spitzer-Härm [39] electron conduction formula along the field line and neglecting T_f as a small number:

$$T_u = \left(T_f + \frac{7}{2\kappa_{e0}} \int_f^u q_\parallel ds_\parallel\right)^{2/7} \approx \left(\frac{7}{2\kappa_{e0}} \int_f^u q_\parallel ds_\parallel\right)^{2/7}. \tag{9}$$

It can be seen that T_u increases with $L_\parallel$ by increasing the $q_\parallel$ integral. An intuitive explanation is that the additional connection length poses a greater resistance to conduction and requires a steeper temperature gradient, increasing T_u for a small, constant T_f. This increases target density due to the assumed constant upstream density and upstream pressure, which in turn enhances radiative power:

$$Q_{rad} \propto n_f = \frac{T_u n_u}{T_f} \propto L_\parallel^{2/7}. \tag{10}$$

As detachment access is proportional to Q_{rad}, this simple, conduction-driven picture yields $K_{L_\parallel} = 2/7 = 0.29$. This dependency is explicitly included in the two-point model [40].

4.5. Benefit of $L_\parallel$ in literature

The classical $K_{L_\parallel}$ scaling is ubiquitous among two-point model implementations [40, 12, 41, 13] but first-principles mechanisms for stronger effects have not been studied as widely. The original DLS paper [13] showed a stronger scaling if $L_\parallel$ is increased exclusively through L_{div},

even without the presence of any radiation. This is because in the DLS and DLS-Extended models, $q_{\parallel}$ above the X-point is assumed to be a linear ramp, leading to greater average $q_{\parallel}$ in the divertor region on average. This means lengthening L_{div} leads to a proportionately greater $q_{\parallel}$ integral increase than if the entire length was increased equally. However, the ballooning nature of radial transport may bias heat flux towards the midplane, as seen in the STEP SOLPS results in Appendix B, which could negate this effect.

The work of Reinke et al. [12] found that the Lengyel integral of the impurity cooling curve cannot be assumed as constant if the radiation is broad, leading to radiation-driven $K_{L_{\parallel}}$ enhancement with $K_{L_{\parallel}} = 3/7 = 0.43$ (see eq. 10 in [12]). This is due to midplane radiation. A narrow-radiating impurity will feature a compact radiation region far from the midplane, which is unaffected by lengthening the flux tube. However, if the radiation fills the flux tube up to the midplane, lengthening it increases the overall radiating volume, provided that the impurity can still radiate at the new, higher upstream temperature. While the study observed this effect to strongly scale with cooling curve width, the resulting model made a simplifying assumption of $L_z \propto T_u$. While not explicitly described as such, this effect is also likely behind the impurity-dependent enhancement of $K_{L_{\parallel}}$ found in the Kallenbach detachment qualifier model [25], leading to an equivalent of $K_{L_{\parallel}} = 0.31$ for argon, assuming $p_0 \propto {L_c}^{2/7}$ - See equation 9 and table 1 in [25]. The same effect is observed in the DLS-Extended results in section 6.2.4 where it is referred to as effect γ.

Several experimental and simulation studies found an enhancement over the classical scaling even without seeded impurity radiation. TCV experiments in lower single null, Ohmic, L-mode unseeded discharges [16, 18, 26] observed an additional effect where increasing L_{div} leads to more SOL broadening, reducing $q_{\parallel}$ and leading to an increased $K_{L_{\parallel}} \approx 0.60$. This was ascribed to asymmetrical broadening in the divertor region which remains poorly understood. Broadening appears to be an important effect, and its inclusion was necessary in the detachment qualifier model to match experiment [25] and in the 1D code DIV1D to match 2D simulations [42]. The lack of analytic models of turbulent broadening means that its inclusion in simple models depends on empirical factors. For this reason, it is not yet included in DLS-Extended whose development so far has been focusing on theory-led fundamental physics investigations, not matching experiment.

A similar enhancement of $K_L \approx 0.60$ was seen in the slab geometry study of Cowley [4] comparing SOLPS-ITER to the original DLS model in narrow-radiating fixed-fraction nitrogen radiation. While the mechanism was unclear, it was driven by changes in pressure drop due to hydrogenic reactions or cross-field transport. A detailed analysis is available in the Cowley thesis [30].

Finally, as mentioned in the previous section, the recent experimental comparison of DLS predictions in unseeded MAST-U experiments shows the importance of both f_R and $L_{\parallel}$ [23] but more work is required to separate the effects and repeat the study with impurity seeding.

In summary, several mechanisms for $K_{L_{\parallel}}$ enhancement have been observed in simulation

and experiment, including ones that are not yet well explained. The mechanism most relevant to the present work is the radiation driven enhancement introduced in [12, 25], whose effect is explored in detail in section 6.2.4. However, there remains a lack of dedicated simulation and experimental studies to validate this effect in isolation.

4.6. Poloidal flux expansion and increasing $L_\parallel$ through magnetic pitch

Throughout most of this work, an increase of $L_\parallel$ is assumed to be driven by a greater poloidal connection length L_θ, but this can also be achieved through lowering the field line pitch angle by poloidal flux expansion (the increase of B_θ, often abbreviated as f_X), such as in the X-divertor concept [43]. This can be represented in DLS-Extended as an $L_\parallel$ increase, and therefore does in principle allow the inclusion of f_X in the study.

However, experiments have found the impact of $L_\parallel$ increasing through f_X on detachment access to be significantly weaker than expected. A dedicated series of SOLPS-ITER simulations was performed in the work by Covele [19] which compared a standard divertor (SD), an X-divertor (XD) with a higher $L_\parallel$ through poloidal flux expansion near the target, and a configuration with the same $L_\parallel$ increase but through a uniform reduction in magnetic pitch throughout the connection length (SDL) to isolate the effect. In this way, the SDL increases only $L_\parallel$ and the XD additionally provides poloidal flaring (i.e. a gradient in pitch angle). The SDL was found to have an increased T_u just like one would expect from the $K_{L_\parallel}$ dependency, but with a corresponding weak threshold improvement of only approx. 10% compared to the expected $\approx 30\%$ from the T_u difference. The reasons remain poorly understood, and more work is required to investigate this effect - ideally in a tightly baffled configuration which would minimise the impact of flows and maximise conduction so that at least the presence of the classical conduction-driven $K_{L_\parallel} = 2/7$ effect can be confirmed.

Increasing f_X appears to have additional benefits, having been shown to improve detachment in some studies [19, 44] but not in others [15]. However, the mechanism is not yet well understood, with one of the leading theories relating to the increase of the volume of plasma that interacts with neutrals and wall-sputtered carbon [19, 45]. This is because both neutrals and wall carbon reside a set poloidal distance from the wall, so that a shallower field line angle allows more interaction. Since DLS-Extended features no neutral physics or sputtering, it is unable to consider these effects, making a realistic assessment of f_X out of scope for the present work.

5. Quantifying influence of magnetic geometry on detachment sensitivity

5.1. Detachment window

The divertor design should ensure that that detachment access is as easy as possible, e.g. achieved with a low plasma density, high power or low impurity fraction. The resulting detachment front location should be insensitive to upstream conditions, so that it is easy for the control system to maintain its location constant. Since the front operational space

lies between the target (reattachment) and the X-point (escape [46]), a controllable divertor should accept a large variation in C between those two extremes. This is captured by the detachment window, first introduced in [13] and defined as the ratio of C at the X-point to that at the target (threshold):

$$W = \frac{C_X}{C_t} \tag{11}$$

A wide window is desirable, e.g. a window of 2 allows the control variable to double before the front escapes into the core. A reduction in detachment threshold widens the window, making improvements to one directly proportional to improvements in the other, assuming no changes above the X-point. An improvement in detachment window is often inversely proportional to an improvement in detachment threshold, since the window is defined as C_X/C_t, the threshold as C_t, and C_X is constant unless upstream magnetic geometry is changed.

A detachment window of less than one indicates the lack of a stable detachment solution: detachment is easier to obtain at the X-point instead of the target. This is easily possible in the inner divertor where sufficient total flux compression causes a decrease of $q_\parallel$ from the target to the X-point, making a detaching front instantaneously move to the X-point. This phenomenon was first described in [13], is evaluated and reproduced in slab SOLPS geometry in [4] and has recently been explored experimentally on MAST-U [47].

5.2. Local sensitivity

The detachment window is only a coarse measure of sensitivity, which can vary throughout the divertor leg. Front location sensitivity, the namesake of the DLS model, can quantified as ds/dC, i.e. the front movement distance for a given change in C (see [4] for an analysis using the original DLS model). Typically, the poloidal sensitivity ds_θ/dC is used due to the diagnostics operating in the poloidal plane. To quantify the influence of magnetic geometry on the sensitivity, we introduce the analytical DLS picture [4]:

$$\frac{ds_{\theta,f}}{dC} = \frac{1}{C}\left[K^S_{f_R}\left(\frac{1}{B_f}\frac{dB_f}{ds_{\theta,f}}\right) + K^S_{L_\parallel}\left(\frac{1}{L_{\parallel,f}}\left(\frac{B_f}{B_{\theta,f}}\right)\right)\right]^{-1}, \tag{12}$$

Where C can be substituted for upstream density as per equation 7 while $K^S_{f_R} = 1$ and $K^S_{L_\parallel} = 2/7$ in the thin radiation limit. The equation contains three key effects:

- $\frac{1}{B_f}\frac{dB_f}{ds_{\theta,f}}$: The B field gradient often dominates parallel sensitivity: in the outer, B increases towards the X-point, reducing the radiative power as the front moves up the leg and stabilising its movement. The reverse is true for flux compression in the inner, which can make the detachment unstable (see sections 5.1 and 7.1.3) The steepness of the B gradient determines the strength of the effect.

- $\frac{1}{L_{\parallel,f}}$: The front becomes more stable as it approaches the X-point due to the reduction of the effective connection length, which makes detachment more difficult due to the classical 2PM effect (see section 4.4.
- $\frac{B_f}{B_{\theta,f}}$: The front becomes more stable *in the poloidal direction* as it approaches the X-point due to a reduced magnetic pitch, requiring more revolutions around the tokamak for a given poloidal distance.

Detailed investigation into the impact of radiation distribution on $K^S_{f_R}$ and $K^S_{L_\parallel}$ is left for future work. DLS-Extended is used to evaluate the sensitivity for selected STEP divertor leg profiles in section 7.2 for completeness.

While detachment sensitivity has been less studied than detachment access, the key mechanisms in equation 12 have been observed in both simulation and experiment. The work by Cowley et al. in [4] and by Cowley in [30] directly compared the predictions of the original DLS model to SOLPS-ITER slab simulations, finding that the DLS predicted more sensitive front movement, but captured the trends in impact of poloidal flux expansion. Experimental work on TCV also found a clear effect of increased poloidal flux expansion reducing poloidal front movement sensitivity [15]. The discrepancy between the analytical DLS model and the slab simulations could have been due to cross-field transport or other effects and demands more investigation. The same slab comparisons observed flux compression (often found in inner divertor legs) leading to an unstable detachment front, an effect first described in the DLS model. The same phenomenon has been observed in experiments on MAST-U [47].

6. Impact of radiation distribution on detachment access

In this section, the four mechanisms controlling the influence of f_R and $L_\parallel$ on detachment access in DLS-Extended are exposed by rearranging the model equations into an integral form divided into four terms. The terms are then evaluated using impurity cooling curves of different width, revealing that K_{f_R} and $K_{L_\parallel}$ can be substantially affected by the size of the radiation region.

6.1. Separating the four effects

We begin by repeating the DLS derivation in [4, 30] without assuming a thin radiation region. This results in an equation for the control variable required for the front to be in a particular location, but now cast in an integral form which can be evaluated using an existing DLS-Extended solution:

$$\frac{\sqrt{f_\alpha} n_u}{Q_{in}^{5/7}} = B_{eff} \frac{Q_{in}^{2/7}}{T_u} \frac{\sqrt{2 \int_X^u \frac{q_{||}}{Q_{in} B^2} ds_\parallel}}{\sqrt{2 \int_{T_f}^{T_u} \kappa_{e0} T^{1/2} L_\alpha(T) dT}}. \tag{13}$$

This equation can be rearranged for either upstream density, power input or impurity fraction required at detachment threshold, with the effects broken down into distinct terms.

The term B_{eff} is a key parameter - the radiation-averaged total B field. It captures the fact that radiation occurs throughout the field line which has a varying B field strength, and reduces to the B field at the front location B_f when the radiation region is infinitely thin. It is calculated as:

$$B_{eff} = \sqrt{\frac{q_{\parallel} Q_{rad}}{q_{\parallel} Q_{rad}/B^2}} = \frac{\sqrt{2\int_{T_f}^{T_u} \kappa_{e0} T^{1/2} L_{\alpha}(T) dT}}{\sqrt{2\int_{T_f}^{T_u} \frac{\kappa_{e0} T^{1/2} L_{\alpha}(T)}{B^2} dT}}. \tag{14}$$

For the full derivation, see Appendix D. Each term in equation 13 is assigned a symbol such that:

$$\frac{\sqrt{f_{\alpha}} n_u}{Q_{in}^{5/7}} = \alpha\beta\gamma\delta, \tag{15}$$

Where α corresponds to B_{eff}, representing total flux expansion effects, β to $\frac{Q_{in}^{2/7}}{T_u}$ which describes heat flux profile effects, γ to $\left(\sqrt{2\int_{T_f}^{T_u} \kappa_{e0} T^{1/2} L_{\alpha}(T) dT}\right)^{-1}$, covering changes to the Lengyel integral and finally δ which corresponds to the term $\sqrt{2\int_X^u \frac{q_{||}}{Q_{in} B^2} ds_{\parallel}}$ which represents the impact of upstream radiation. Each term is described in detail in the following sections.

6.2. Quantifying the effects

The impact of each term on the benefit of total flux expansion (K_{f_R}) and connection length ($K_{L_{\parallel}}$) was assessed by taking the baseline simulation from section 3 and increasing the connection length and total flux expansion by a factor of 2. This was achieved by modifying the B_{tot} profile below the X-point, leaving the upstream unmodified. Density was chosen as the upstream condition output for simplicity, with overall K_{f_R} and $K_{L_{\parallel}}$ calculated by comparing the upstream density required for detachment threshold before and after each change in leg geometry according to equation 11. The results were used to evaluate the contributions of each of the four terms in equation 13, with the following example for calculating the contribution of term α to K_{f_R}:

$$K_{f_R,\alpha} = -\frac{log_{10}\left(\frac{\alpha_2}{\alpha_1}\right)}{log_{10}\left(\frac{f_{R,2}}{f_{R,1}}\right)}, \tag{16}$$

This is repeated for the other three terms and the same procedure applied to $K_{L_{\parallel}}$. The overall scaling factor is the sum of each of the four contributions, e.g. $K_{f_R} = K_{f_{R,\alpha}} + K_{f_{R,\beta}} + K_{f_{R,\gamma}} + K_{f_{R,\delta}}$. The procedure was used to evaluate a number of cooling curves in order of increasing width: an arbitrary analytical thin curve, argon in the coronal approximation, the effective argon curve extracted from SOLPS (see section 3), non-coronal argon and non-coronal neon. The non-coronal argon and neon curves assumed $n_e\tau = 5 \times 10^{-19}\mathrm{m}^{-3}\mathrm{ms}$, just like the constant $n_e\tau$ curve in section 3 (see Appendix B.1 for more detail).

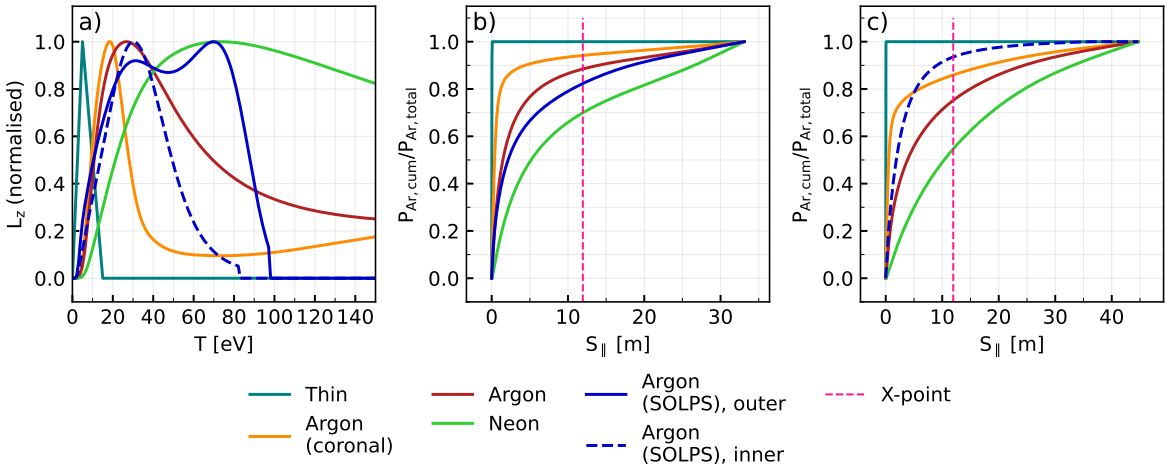

Figure 2: a) Cooling curves (normalised for clarity), b) cumulative radiation distribution for the outer divertor, c) cumulative radiation distribution for the inner divertor.

The curves and the resulting radiation distributions are shown in figure 2. Since the SOLPS curves are extracted from a simulated flux tube with a certain temperature range, they feature artifacts near the high temperature end - there is a rapid reduction in L_z followed by a sharp cut-off. Unlike the other curves in the study, this makes the SOLPS curves unable to radiate beyond the original SOLPS simulation upstream temperature. This artifact affects the results, as outlined in section 6.2.6. The outer divertor curve additionally features a broad double peak, which cannot be captured with a constant $n_e\tau$ curve. See Appendix B.1 for additional discussion of these features.

The results showing K_{f_R} and $K_{L_\parallel}$ as predicted by DLS-Extended for the STEP divertor are shown in figure 3. Each bar is composed of individual scaling factors corresponding to each of the four terms, which together add up to the overall proportionality constant shown by the value at the top of each bar. It can be seen that the radiation effects have a significant, nonlinear impact on the role of total flux expansion and connection length in detachment access. K_{f_R} is significantly reduced through term α as radiation broadens, especially in the inner divertor. Meanwhile, $K_{L_\parallel}$ is significantly increased by term γ for the widest cooling curves. This is offset by a small reduction in term δ, while term α improves detachment for the outer and worsens it for the inner. The key results are analysed in the following sections.

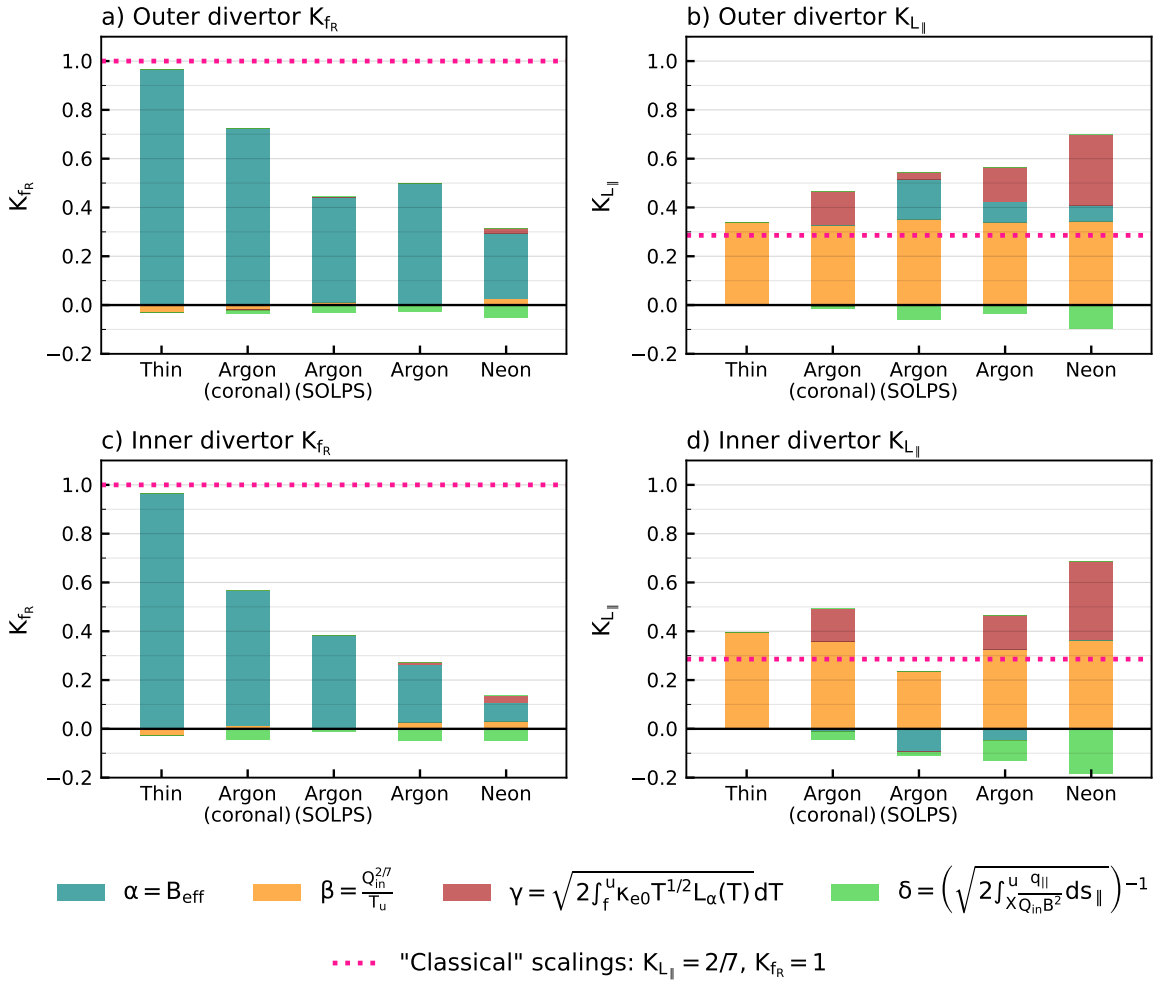

Figure 3: Detachment access proportionality constants K_{f_R} (left) and $K_{L_\parallel}$ (right) obtained by observing the impact of doubling f_R and $L_\parallel$ on DLS-Extended results. This is repeated for several cooling curves for the outer (top) and lower (bottom) divertor. Each colour bar represents the proportional contribution from one of the four physical effects. The cooling curves are arranged by width in an ascending order from left to right.

6.2.1. Performance with the thin curve In the total flux expansion results, the thin curve matches the classical scaling of $K_{f_R} \simeq 1$ due to having a negligibly wide radiation region. The small deviation from $K_{f_R} = 1$ is due to f_R changing the $q_\parallel$ profile (see section 4.2) and so manifests as a contribution of the β term. In the case of connection length (figures 3b and 3d), $K_{L_\parallel}$ is higher than the classical 2/7 due to having increased L_{div} while keeping the upstream connection length constant, which leads to a stronger scaling as explained in section 4.4.

6.2.2. Term α: total flux expansion The most striking effect seen in figure 3 is the dramatic reduction of K_{f_R} as radiation becomes more broad through the use of wider cooling curves (roughly ordered from left to right). This is due to more radiation loss taking place upstream where the B field is greater, and so $q_\parallel$ is higher. This can be thought of as radiation "averaging out" the variation in the B field profile, reducing effective f_R:

$$f_{R,eff} = \frac{B_X}{B_{eff,target}}, \tag{17}$$

Where B_{eff} is the radiation-averaged B field, or term α. As radiation narrows, $B_{eff,target} \rightarrow B_{target}$ and $f_{R,eff} \rightarrow f_R$, as illustrated for the outer divertor in figure 4a. Radiation broadening can slightly mitigate this effect if there is more radiation upstream, as shown in figure 4b, but this is observed to be a minor effect. Figure 3b) shows that term α not just diminishes K_{f_R} but also enhances and reduces $K_{L_\parallel}$ for the outer and inner divertor, respectively. This is because as the connection length increases, the radiation region becomes a smaller proportion of the domain while simultaneously slightly shrinking due to the steeper temperature gradient. This reduction in radiation region size undoes the impact of effect α, increasing $f_{R,eff}$ in the outer and decreasing $f_{R,eff}$ in the inner, improving and worsening detachment access, respectively.

The inner divertor features flux compression, which reduces detachment performance in the exact but opposite way to the flux expansion seen in the outer leg. Since flux compression is simply when f_R is less than unity, the strength of its effect is described by the coefficient K_{f_R} in the same way as for flux expansion. This means that the K_{f_R} reduction in the inner target is actually beneficial and helps to stabilise the detachment front (see section 7.1).

Another difference in the inner divertor is its generally greater propensity for broad radiation. Unlike the outer, the inner leg features no low B region to help with $q_\parallel$ dissipation, and its divertor region is a smaller proportion of the overall connection length. This effect is responsible for the overall stronger K_{f_R} reduction for the inner. To help illustrate the impact of effect α on f_R, table 1 shows the values of $f_{R,eff}$ in both the inner and outer divertors. The thin curve preserves the original $f_R = 2$, while broader curves reduce it significantly, particularly for the inner leg which shows a near-complete reduction when using neon.

6.2.3. Term β: heat flux profile The term $\beta = \frac{Q_{in}^{2/7}}{T_u}$ represents T_u effects given a constant Q_{in}. This means it responds to any changes in the $q_\parallel$ profile which affect the $q_\parallel$ integral

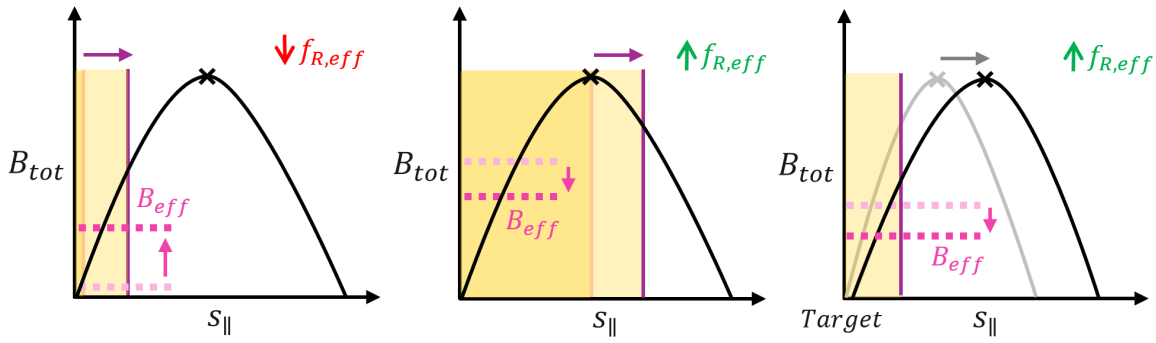

Figure 4: Effects caused by term α due to the "radiation averaging" of the B field in an outer divertor. a) Broadening radiation below the X-point increases B_{eff}. b) Broadening radiation above the X-point can counteract this and reduce B_{eff} (this is a small effect). c) Increasing connection length reduces B_{eff}.

Table 1: Impact of cooling curve choice on $f_{R,eff}$ in each divertor leg.

Side	Parameter	Thin	Argon(coronal)	Argon	Neon	SOLPS
Outer	$f_{R,eff}$	2.00	1.72	1.44	1.25	1.38
Inner	$f_{R,eff}$	2.00	1.54	1.22	1.09	1.32

due to the dominating influence of electron conduction. Therefore, the term β is mostly comprised of the classical effect of T_u increasing with $L_{\parallel}$ (see 4.4), but also captures other mechanisms which have a smaller, but non-negligible impact on the $q_{\parallel}$ profile - radiation and total flux expansion.

It can be seen in figures 3b) and 3d) that the thin curve does not match the classical scaling of $K_{L_{\parallel}} = 2/7$, even though it has no radiation-driven effects. This is because $L_{\parallel}$ was increased through L_{div}, which has a higher average $q_{\parallel}$ than the upstream region in DLS-Extended due to its assumption of a uniform upstream heat source. This leads to a proportionally higher $q_{\parallel}$ integral compared to lengthening the entire domain evenly (see section 4.4). This small effect may disappear if a more realistic upstream heat source profile is used, as cross-field transport is stronger at the midplane in SOLPS (see Appendix B for a comparison). The small variations in term β for both K_{f_R} and $K_{L_{\parallel}}$ are due to minor changes in the heat flux profile due to different radiation distributions, as well as due to any differences in the average B field in the divertor region (see section 4.2).

6.2.4. Term γ: radiating volume This term represents the Lengyel integral, which integrates the cooling curve along the domain to to obtain radiative power. This can be done analytically in the thin radiation limit where the integral is a constant, e.g. in [10], [4]. This approach breaks down in the case in broad radiation, as first described in [12]. A thin

radiation region prevents any radiation upstream, making the Lengyel integral insensitive to lengthening the domain as the additional connection length is not used for radiation. However, if the cooling curve is wide enough to produce radiation at tempereatures higher than T_u, then upstream radiation persists after the flux tube is lengthened, and radiative volume is increased. This makes the Lengyel integral scale with $L_\parallel$ according to some proportionality coefficient, which depends on the cooling curve used [12].

This effect is responsible for the significant enhancement of $K_{L_\parallel}$ shown in figure 3 for curves with a high shoulder (high temperature) region, particularly neon (see 2). No enhancement for the SOLPS-extracted curve can be seen due to the fact it terminates at T_u, which is an artifact of extracting a curve in this way - the underlying simulation has no data beyond the upstream. In reality, it could look more similar to the non-coronal argon curve. Interestingly, both the coronal and non-coronal argon curves perform similarly, likely because they converge at high temperature (see figure 2).

6.2.5. Term δ: upstream radiation This term is a consequence of rearranging the equation to obtain the other terms and has limited interpretative value. It captures anything that affects how much $q_\parallel$ makes it to the divertor region: a key example is a reduction in upstream radiation increasing the $q_\parallel$ that must be dissipated downstream in the divertor region. Its impact on the results in figure 3 is always negative, as increasing $L_\parallel$ and f_R both lead to a reduction in upstream radiation. The effect is strongest for the inner divertor which generally features more radiation above the X-point, and for the broadest radiating impurities.

6.2.6. SOLPS curve effects As shown in figure 2 and discussed in section 3 and Appendix B.1, the SOLPS extracted curves have artifacts which distinguish them from the ADAS data - they rapidly decay towards the upstream temperature where they experience a sharp cut-off, and the outer curve features a double peak. It is not possible to choose a constant $n_e\tau$ parameter to match either feature. The high temperature cutoff prevents radiation from increasing at greater $L_\parallel$, minimising the influence of effect γ and δ for both divertors, as shown in figures 3b) and 3d). This contributes to an unusually low $K_{L_\parallel}$ for the inner divertor. Effect α is another contributor: the SOLPS curve features a smaller amount of radiation above the X-point than the other curves (see 2), which causes the narrowing of the radiation region relative to L_{div} cause a greater weakening of the "averaging out" effect and recover more flux compression. Finally, unlike the others, the SOLPS curve features a lower effect β than the classical scaling. This is because of the greater effective flux compression increasing $q_\parallel$ in the divertor region. In section 7.1 a strike point position scan is performed instead of artificially increasing $L_\parallel$ and f_R individually, where the inner shows to have a significantly higher $K_{L_\parallel}$ than it appears in this study. The reasons for this are still not well understood, but are likely to do with the abrupt cut-off seen in the SOLPS curves. In the outer divertor, the influence of effect α is increased in both K_{f_R} and $K_{L_\parallel}$ due to the double peak feature (figure 2) leading to a very broad curve in the mid-temperature region.

The reason why the SOLPS results are distinct from the ADAS curves is due to the differences in the curves themselves, which are not yet well understood. For example, it is not clear why the outer would feature a double peak and if this is a general feature of STEP, and whether it disappears when different puffing configurations or equilibria are used. It is also unknown why the cooling curve would feature a rapid drop before the high temperature cut-off, and how the cut-off would respond to increases in parallel connection length. Further study is needed to understand these impurity transport effects, but this must be done using high-fidelity modelling tools and is out of scope for the present work. These effects highlight the challenges in using simple models which must rely on fixed radiation curves.

7. Impact on divertor design

Section 6 provided an in-depth analysis of the radiation effects, but the study was unrealistic from a divertor design standpoint: f_R and $L_\parallel$ were changed in isolation, while in reality moving the strike point changes both simultaneously. To address this, section 7.1 features a strike point location scan for both inner and outer divertors using the "thin" and "SOLPS argon" curves only, capturing the impact on detachment access and detachment window. In section 7.2, selected profiles are further analysed to reveal the entire front movement profile during a density scan, capturing front location sensitivity along the field line. Finally, section 8.2 summarises the implications for the initial STEP divertor design studied in this work.

7.1. Strike point location scan

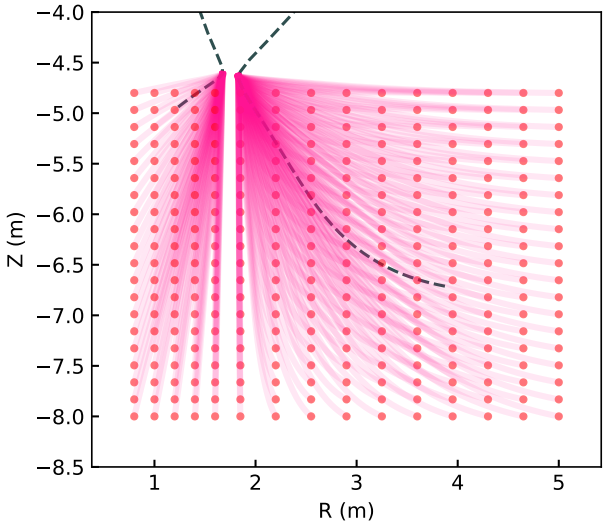

Figure 5: Divertor leg profiles

Figure 6: The baseline divertor leg profile (dashed) and the new profiles (pink).

7.1.1. Simulation setup The baseline DLS-Extended calculation was used as a basis for the new analysis of 150 different potential strike point locations and leg geometries shown in fig. 6, which were calculated by assuming $B_{tor} \propto R^{-1}$, $B_\theta / s_\theta = const$ (where s_θ is the poloidal distance along the field line) and no changes above the X-point. The SOLPS-extracted cooling curve was used along with the conditions from the baseline case with a tuned conductivity from section 3 to be as representative of the SOLPS simulations as possible. Each geometry was simulated with the front at the target to calculate the detachment threshold, and once again at the X-point to obtain the window. The results were repeated using the thin curve to show the impact of broad radiation.

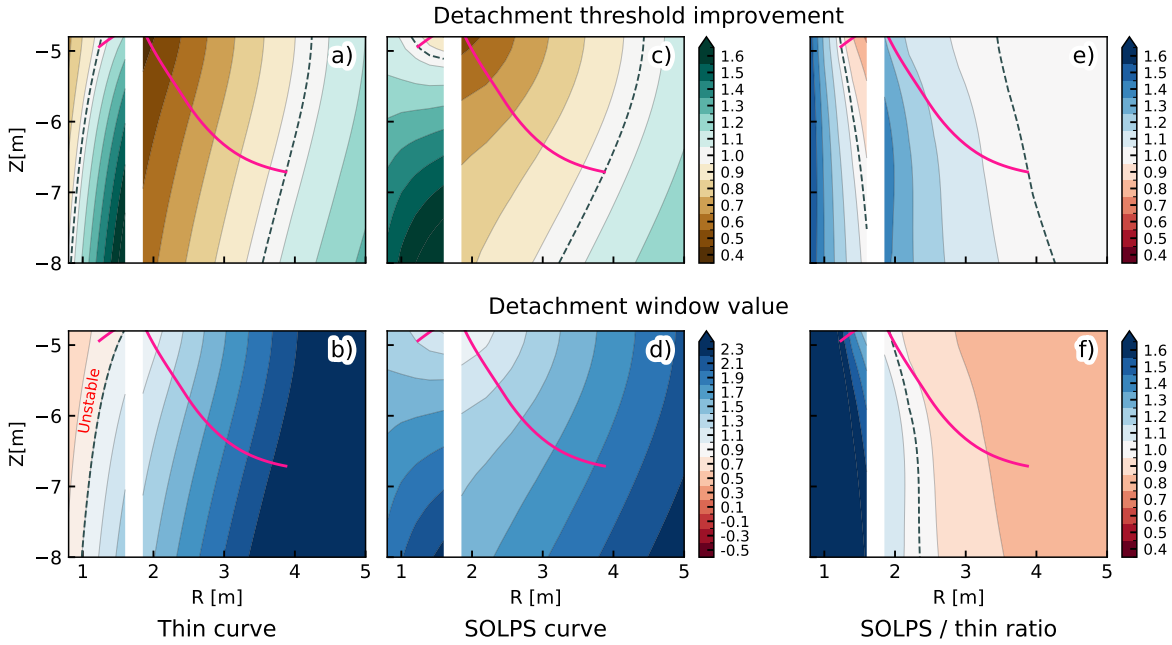

Figure 7: Effect of moving the strike-point position on detachment performance with the thin cooling curve: a) Improvement to detachment threshold and b) the absolute value of the detachment window. This is repeated for the argon curve in c) and d), respectively, showing the impact of broadening radiation. The final column in e) and f) show the ratio of the argon to thin curve results for the detachment threshold improvement and detachment window value, respectively. The baseline divertor leg profile is shown in pink.

7.1.2. Impact of radiation on detachment access Figures 7a and 7c show the detachment threshold improvement factor for different strike point positions when using the thin and SOLPS argon cooling curve, respectively. The threshold improvement is relative to the baseline divertor leg profile shown in pink in the same figure, and a value of 1.1 corresponds to a 10% reduction in upstream density to reach detachment. When the thin curve is used, both the inner and outer legs show high sensitivity to horizontal strike point movement due to a high K_{f_R} and low $K_{L_\parallel}$. Using the SOLPS argon curve reduces K_{f_R} and increases $K_{L_\parallel}$ through mechanisms identified in section 6.2, which is apparent in figures 7c and 7d through the colour bands becoming rounder and less vertical due to the stronger dependence of detachment threshold on connection length. Figure 7e shows the ratio of the SOLPS to the thin curve, confirming that the main effect is the reduction of sensitivity to horizontal strike point movement, improving detachment access at low major radius.

In the outer divertor, this amounts to a 38.4% reduction in horizontal movement sensitivity. This reduction is less than could have been expected from the simpler tests in section 6 because moving the strike point outwards changes both f_R and $L_\parallel$ simultaneously. The inner divertor sees a dramatic change, being almost completely dominated by the impact of connection length. This is in contrast to the simpler study in section 6.2, where both K_{f_R} and $K_{L_\parallel}$ featured a large reduction with K_{f_R} still dominating overall. This implies a nonlinear interplay between f_R and $L_\parallel$ effects when both are changed together in a more realistic fashion.

7.1.3. Impact of radiation on detachment window Detachment access is insufficient to capture detachment performance alone. It is possible for a divertor design to feature easily accessible detachment, but with a narrow operating space between reattachment and escape into the core. The size of this operational space is captured by the concept of the detachment window (defined in section 5.1), which is a crude, 0D measure of detachment front sensitivity.

Figures 7b) and 7d) show the results. Unlike the plots of detachment threshold, the detachment window is shown as an absolute value instead of an improvement ratio. This is to highlight regions where the window is lower than unity which indicate the lack of a stable detachment solution (see section 5.1). The window value corresponds to the size of the stable region, but does not guarantee stability at every point of the field line, which is explored in the following section. As expected, the contours look visually similar to ones showing the improvement in detachment threshold (figures 7a and 7c) because improvements in window are proportional to improvements in detachment access (see section 5.1). The different quantitative value of the ratio of the two curves (figure 7f) is due to the window being shown as an absolute value, unlike the detachment threshold improvement which is a ratio.

DLS-Extended predicts the baseline inner divertor to be unstable when using the thin curve (as shown in figure 7b). This is due to flux compression reducing $q_\parallel$ towards the X-point, making the detachment front solution easier to achieve at the X-point than at the target. The contours show that a small, stable window can be regained by moving the inner

strike point towards the outboard. Using the SOLPS argon curve makes every strike point location feature a stable region, leaving a modest detachment window of approx. 1.3, i.e. the upstream density can only be increased by 30% after the onset of detachment before it reaches the X-point. This improvement is due the wide radiation region reducing effective flux compression. The SOLPS curve also significantly reduces the sensitivity to horizontal strike point movement which appears stronger than that shown in the simple study in section 6.2. The outer divertor becomes less stable: the baseline detachment window reduces by 17.6% and the sensitivity of the window to the horizontal strike position reduces by 49.8%. This is due to the same effect as the stabilisation of the inner, but in reverse - a broad radiation region reduces effective flux expansion.

7.2. Detachment front location scan

While the detachment window results shown in figure 7 show the size of the stable operational space, the window is too crude a measure to identify local front movement sensitivity in different regions along the field line. To evaluate this, DLS-Extended was used to perform a front location scan for a number of selected geometries shown in figure 8a. The geometries were prepared in the same fashion as in the strike point location scan, i.e. interpolated onto new R,Z coordinates without requiring a different equlibrium. The outer strike point has been moved up, down, radially inwards and radially outwards by one metre, while the inner strike point has been moved a small distance radially outwards, and then halfway towards and in line with the outer target. For each divertor geometry, an upstream density scan was performed to predict the evolution of the poloidal detachment front position. The results are shown in figures 8b-e, featuring both the inner and outer divertors, each with the thin and SOLPS argon curves. The plots show the poloidal movement of the front in response to upstream density changes, which are shown on a relative basis, where an upstream density increase ratio of 1 corresponds to the density needed for detachment onset.

The gradient of the front movement curve indicates sensitivity, where a steeper slope implies a greater front movement in response to upstream density change. While the extent of the curve along the Y axis is the poloidal connection length, the X axis extent is the detachment window. It can be seen that using a broad curve reduces the window for the outer divertor and increases it for the inner divertor, as shown in figure 7 and explained in section 7.1. For each divertor geometry, the detachment front is less sensitive near the X-point and more sensitive near the target. This is because of the two effects described in section 5.2:

- The magnetic pitch reduces around the X-point, requiring more parallel front movement for each unit of poloidal distance.
- The further the front is from the target, the less connection length remains upstream; moving it further results in a greater proportional decrease of the remaining connection length.

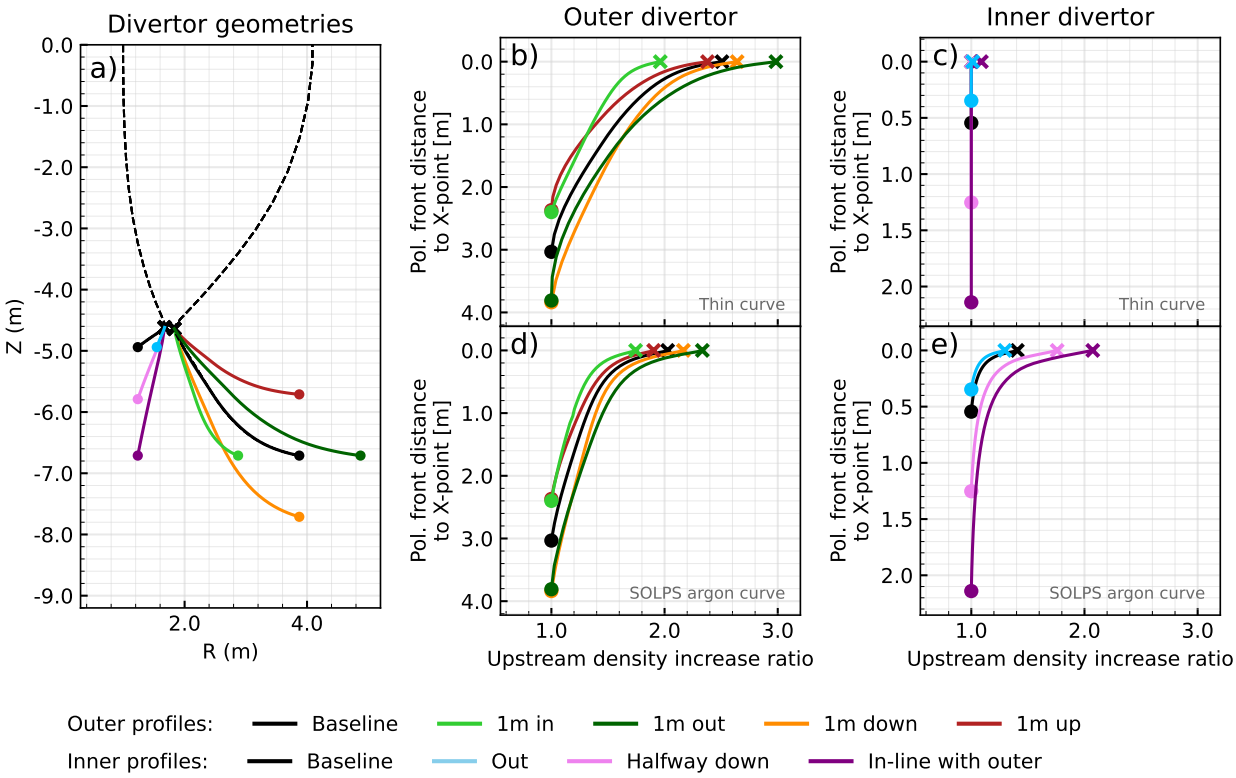

Figure 8: Front location scans with respect to upstream density for selected divertor geometries. Targets are marked with a dot, and X-points with an X. The geometries are shown in a). The outer and inner scans for the thin curve are shown in b) and c), respectively, and the scans for the SOLPS argon curve are presented in d) and e).

The third effect introduced in section 5.2 is the stabilising influence of the B field gradient. In the results shown in figure 8, this results in the inner divertor being significantly more unstable near the target due to its lack of flux expansion.

Each studied geometry results in a different front movement profile. In each of the studied cooling curves for the outer divertor, moving the strike point radially outwards gives the greatest detachment window due to f_R and $L_\parallel$ increasing simultaneously, while moving it inwards gives the smallest window due to their simultaneous decrease. Moving the strike point vertically by the same distance has a reduced effect due to only $L_\parallel$ changing and f_R staying constant. Moving from the thin to the SOLPS argon curve not only reduces the detachment window and increases movement sensitivity for all profiles, but also reduces the variation in local sensitivity between each geometry due to the broad radiation averaging out the B field variation.

Consistent with the predictions from section 7.1 shown in figure 7, the inner divertor is either unstable or marginally stable in all of the chosen geometries when the thin curve is used. Introducing a realistic curve substantially increases the extent of the stable region

due to the lower effective flux compression. The same effect reduces the sensitivity to changes in f_R, resulting in $K_{L_\parallel}$ having a dominating effect, as shown by moving the strike point outwards (blue profile) worsening the window due to the lower $L_\parallel$ even though flux compression is reduced. While moving the strike point downwards results in an improvement in detachment window, most of the extra connection length is not "useful" due to being marginally stable: both the in-line (purple) and halfway (violet) strike point geometries feature very high sensitivity if the front is more than 0.5m away from the X-point.

8. Recommendations and discussion

8.1. Model validation

The original DLS model's predictions of detachment threshold are nothing more than saying that $K_{f_R} \simeq 1$ and $K_{L_\parallel} = 2/7$. This means "validating" the DLS model can be done by confirming those coefficients. As described in detail in section 4), this has now been done across several simulation and experimental studies, giving confidence in the simple magnetic geometry effects underpinning the DLS models even though K_{f_R} and $K_{L_\parallel}$ can also be affected by mechanisms not included in the DLS, such as flows [17, 38] and turbulent broadening [26, 21]. Section 8.3 discusses how they could be incorporated into DLS-Extended.

The radiation effects presented in this paper have not yet been the subject of experimental or high fidelity simulation validation, as only the radiation-driven $K_{L_\parallel}$ enhancement (effect γ in section 6.2.4) has previously been reported [12, 25]. The first-principles nature of the analysis in this paper and a comparison of the radiation profile against SOLPS-ITER are clear evidence of the importance of radiation broadening effects, and are a strong argument to motivate further experimental or high-fidelity simulation studies. These must be done with care to ensure the effects are appropriately isolated, e.g. by ensuring tightly baffled conditions. A modelling study is currently ongoing to confirm the radiation distribution findings in a high-fidelity 2D mean-field code.

The validation of the front movement sensitivity is a more niche topic with less relevant study available in literature. As outlined in section 5.2, there have been several comparisons with simulation [4] and experiment [47, 48] showing qualitative agreement. While this gives some confidence in DLS model predictions, more work is needed in this area.

It is important to consider that as a reduced model, DLS-Extended is not intended to provide accurate, quantitative detachment predictions, or be physics-complete. Instead, it is best used to look at relative changes, e.g. between different magnetic geometries. In its current form, DLS-Extended is almost entirely first-principles to maintain interpretability as a framework to understand detachment performance and sensitivity, but can be easily enhanced with e.g. empirical turbulent broadening effects (see section 8.3).

8.2. Recommendations for STEP divertor design

As shown in the detailed breakdown in section 6.2, the more realistic strike point scan in 7.1, and the sensitivity analysis in 7.2, broad impurity radiation can result in the strengthening of $K_{L_\parallel}$, the weakening of K_{f_R} and the decrease and increase in sensitivity in the inner and outer divertors, respectively. The effects strengthen with broader radiation, and so are more pronounced with impurities such as neon compared to narrow-radiating impurities such as nitrogen and can be sensitive to other factors influencing the radiation location, e.g. puff location and the impurity residence time.

For the outer STEP divertor, the radiation effects present in the SOLPS simulations result in an approximately equal benefit of f_R and $L_\parallel$. This means that the original DLS model conclusions remain broadly unchanged: positioning the outer target at the maximum major radius improves detachment access and stability as both f_R and $L_\parallel$ increase. The sensitivity of detachment performance with respect to the vertical strike-point position is much weaker, as it features a smaller change in $L_\parallel$ and no change in f_R.

For the inner divertor, the radiation effects make achieving good detachment access and stability significantly easier due to the reduced effective flux compression. Both the strike-point (section 7.1) and sensitivity (section 7.2) sections show a near total elimination of the impact of f_R, resulting in best performance when $L_\parallel$ is prioritised. Achieving this by moving the strike-point vertically downwards like the inner divertor design of ADX (Advanced Divertor and RF tokamak eXperiment) [49] improves the detachment window, but crucially, the improvements are mostly near the X-point and much of the additional connection length remains marginally stable (see figure 8).

Both the inner and outer divertors are shown to significantly benefit from taking up more space. This means that any actual optimisation of the STEP divertor design must be made with full consideration of the engineering constraints, e.g. the equilibrium, the physical locations of the coils or the overall machine cost. In this way, incorporating DLS-Extended into systems or equilibrium design codes could lead to a better balance of cost to performance.

Apart from strike point optimisation, the results from this work show a new avenue for optimising detachment performance - changing the extent of the impurity radiation, e.g. by changing puff location or the impurity species mix. While these design considerations are primarily driven by other, more important requirements, the new findings could help to find a more optimal configuration. In general, the outer divertor benefits from the narrowest radiation extent, which could be achieved by e.g. puffing as close to the target as possible. The inner benefits from the broadest radiation, but radiation above the X-point can lead to radiation in the core.

Aside from predicting detachment access and window, the DLS models have the ability to predict front sensitivity at any point along the field line (section 7.2). During operation, it is important for the front to be located in a region of low sensitivity to ensure it can be as controllable as possible and stay within the field of view of the diagnostics.

The results show that the front is more sensitive near target than near the X-point in both divertors. This conclusion is similar to the the results of X-point radiator experiments [50], but further work is necessary to confirm the link to the DLS equations. The inner leg is always more sensitive due to the lack of stabilising flux expansion, apart from in negative triangularity [51] configurations. An X-divertor could be used to improve local sensitivity near the target, such as the inner X-divertor configuration explored in later STEP design iterations [32], but obtaining a strong benefit is constrained by the field line incidence angle and the requirement to minimise the number of poloidal field coils near the divertor chamber. Therefore, as with detachment access, the DLS-Extended predictions for front movement sensitivity are best used as part of an integrated systems approach where control, cost and engineering considerations are taken into account simultaneously.

8.3. Outlook and model limitations

DLS-Extended offers a highly transparent, first-principles-based framework for understanding detachment in the presence of radiating impurities. Its simplicity, fast runtime and minimal reliance on arbitrary or empirical tuning parameters make it particularly interpretable and a valuable tool for early-stage equilibrium design and magnetic geometry optimisation.

However, as with all reduced models, there are tradeoffs that require higher fidelity models to assess. The most significant is the lack of particle sinks and mechanisms for energy dissipation besides radiation. Cross-field transport, neutral reactions and even electron-ion equipartition can violate the constant pressure assumption [30]. The impact of cross-field transport due to localised particle sources can also be significant (see Appendix B), but nevertheless allows a reasonable comparison to SOLPS given an appropriate field line choice.

Omitting neutral physics should theoretically make DLS only valid in impurity radiation dominated regimes. However, the majority of the experimental and simulation studies described in sections 4.3 and 4.5 recover the K_{f_R} and $K_{L_\parallel}$ as derived in the original DLS model assuming impurity radiation to be the only loss mechanism. This hints at a possible commonality with hydrogenic loss processes, which also benefit from increased flux tube volume and high n_{target}, allowing the classical effects of f_R and $L_\parallel$ to still work. A self-consistent application of the DLS models to such scenarios is challenging without evolving the neutral population which would add a considerable amount of complexity to the model, bringing it more in line with high-fidelity 1D models such as Hermes-3 in 1D [52] or DIV1D [42], losing its speed and interpretability benefits. Incorporating a reduced neutral model such as the one in [25] could be a viable alternative, but would require adapting to a fully detached condition, i.e. where the "target" boundary is the detachment front.

The treatment of the detachment front boundary condition is also a key limitation of the DLS models. The detachment front is considered as a "virtual target" boundary [13] and requires a non-zero heat flux in order to integrate the ODE equations underpinning DLS-Extended. In reality, a non-negligible convective heat flux remains (one definition of the detachment front is where conductive and convective heat fluxes are equal [4]). This

heat flux was originally proposed [30, 53] to be calculated according to a standard sheath heat transmission formula [40]. However, as there is no reason for the sheath formula to be accurate for a detachment front, the present work simply sets the target heat flux to a low value (see 3). There are at least two additional areas where the physics in DLS-Extended can be improved. Firstly, the impact of electron conductivity reducing with Z_{eff} (see e.g. [12, 32]) is currently omitted, and secondly, the upstream heating source is uniform, preventing a ballooning-like heat flux profile above the X-point (see section 6.2.3 and Appendix B).

The DLS models suffer from the same shortcomings as the other Lengyel models when it comes to the accuracy of absolute predictions of detachment access (e.g. for ITER [10] and DEMO [11]). In a significant recent study [34], the absolute prediction gap has been successfuly closed through the consideration of cross-field transport, neutral losses and turbulent broadening of the heat flux channel, all accounted for in a reduced form by combining the Lengyel [9] and Kallenbach [25] models. Like in the Kallenbach model, this novel, combined approach is valid only up to the point of detachment onset. Since DLS-Extended is effectively a way to adapt the Lengyel approach to deep detachment, there is an opportunity to combine these models together and obtain something which is valid both in attached and deeply detached conditions.

All 1D divertor models suffer from three additional limitations. Firstly, the conclusions can be affected by the choice of flux tube, and it is not known a priori which flux tube is the limiting factor for reattachment. This could be mitigated by some form of onion-skin model [54]. Secondly, 1D models treat each divertor in isolation, while in reality they can share common upstream conditions and can be linked through both the SOL and PFR regions. While DLS-Extended could theoretically be used for combined inner-outer (single null) or inner-inner/outer-outer (double null) divertors to account for the SOL coupling, the PFR coupling demands further study. Finally, inner divertors can feature strong 2D effects due to e.g. neutral physics and drifts [25], making 1D predictions less reliable.

While all reduced models have limitations, they play an important role in divertor design, which is a complex, multidisciplinary challenge requiring a wide range of skillsets as well as a wide range of simulation tools of different computational cost. Simple and computationally affordable tools can reduce the number of iterations between engineers, equilibrium designers and plasma physicists, as well as the number of expensive, high-fidelity simulations. DLS-Extended is open source, written in Python and care has been taken to ensure that it is easy to use and couple to other frameworks.

9. Conclusions

In this work, we introduced DLS-Extended, a new code building on previous work on the Detachment Location Sensitivity (DLS) model [13, 14], including a recent SOLPS-ITER validation of detachment access and sensitivity predictions [4]. Like the original DLS model, DLS-Extended can predict the impact of magnetic geometry and upstream conditions on detachment access as well as front movement in deeply detached conditions. It improves

upon the original DLS model by considering a 1D domain instead of just the upstream and front location points, allowing the prediction of the extent of impurity radiation and relaxing the infinitely thin radiation region assumption. The predictions of radiation distribution were compared against a SOLPS-ITER simulation of an initial STEP design for both the inner and outer divertors, showing good agreement for the chosen SOL rings when the exact cooling curve was used. The agreement is sensitive to cooling curve choice and the presence of density sources, e.g. due to puffing and cross-field transport. The SOLPS simulations showed that STEP features broad radiation.

DLS-Extended was then used to investigate the impact of the spatial distribution of the impurity radiation on the effectiveness of total flux expansion (f_R) and connection length ($L_\parallel$) in enhancing detachment access, expressed as proportionality constants K_{f_R} and $K_{L_\parallel}$. The analysis was performed on both the inner and outer STEP divertors by doubling f_R and $L_\parallel$ individually for a selection of cooling curves: a synthetic thin curve, coronal and non-coronal argon, the effective argon curve extracted from SOLPS and non-coronal neon. It was found that as radiation broadens, it averages out the effective B field variation, reducing K_{f_R}. This is detrimental for the outer divertor, but beneficial for the inner divertor where f_R is negative due to flux compression. The inner divertor sees a stronger effect for the broadest curves due to the divertor region being a smaller fraction of the overall connection length, making upstream radiation easier. Broadening radiation was also found to enhance $K_{L_\parallel}$ primarily due to two effects: firstly, if the curve allows radiation at high temperatures and leads to midplane radiation, lengthening the flux tube increases the volume available for radiation to take place. Secondly, lengthening the flux tube reduces the radiation extent as a fraction of the total connection length, reversing the f_R effect due to B field averaging.

STEP plans to use argon seeding. For both the inner and outer divertors, if the non-coronal argon curve is used, the effects lead to K_{f_R} approximately halving and $K_{L_\parallel}$ approximately doubling, leaving them of similar importance. Using the exact argon cooling curve extracted from SOLPS gives similar results apart from $K_{L_\parallel}$ weakening for the inner. The reasons for this are still unclear, particularly since the following studies showed a stronger $K_{L_\parallel}$ and weaker K_{f_R} for the inner. It is likely due to the fact the curve is clipped to the temperature range seen in the SOLPS simulation, resulting in a high temperature cut-off not present in the other curves.

DLS-Extended was then used to scan a number of strike point locations for both divertors, allowing $L_\parallel$ and f_R to evolve in line with the geometry profile, instead of being artificially changed in isolation. The resulting changes in detachment access and detachment window were compared when using the thin and SOLPS argon curves. Using the realistic curve reduces the outer divertor strike point's sensitivity of detachment access to horizontal movement by approx. 40% due to the combined effect of increased $K_{L_\parallel}$ and decreased K_{f_R}. Unlike the simpler study, the inner divertor is seen to be near completely dominated by $K_{L_\parallel}$ when using the SOLPS curve. This implies that artificially isolating f_R and $L_\parallel$ omits some nonlinear effects which are not yet well understood.

The detachment window results show that the inner has been stabilised and the outer destabilised due to the weakening of the detrimental effect of flux compression and beneficial effect of flux expansion, respectively. However, the detachment window is a crude measure of detachment stability since it doesn't consider how sensitivity evolves along the field line. To address this, selected divertor geometries were analysed through a full front location scan, which confirmed that the inner leg can be most improved by increasing $L_{\parallel}$ (moving the strike point downwards) and the outer leg through increasing $L_{\parallel}$ and f_R (moving the strike point outwards). Both the inner and outer divertors are more stable near the X-point than near the target due to connection length and magnetic pitch effects. This is particularly pronounced for the inner divertor due to its flux compression, resulting in connection length increases widening the stable region 0.5m from the X-point but keeping the downstream region very sensitive.

Accounting for radiation effects changes the importance of vertical compared to horizontal strike point movement, particularly for the inner, which becomes very insensitive to changes in major radius. However, the overall implications for strike point placement are broadly unchanged from the original DLS: both the inner and outer divertors benefit from taking up additional space, and so any design optimisation must be done by balancing this against engineering and cost constraints.

Radiation distribution is more important when considering detachment sensitivity, with the outer divertor detachment window reducing by approx. 20%, and the inner divertor no longer being completely unstable. The inner is significantly affected because detachment stability is very sensitive to flux compression, which is averaged out by radiation spreading throughout the divertor leg. The results show that radiation effects are critical to the understanding of inner detachment stability. The sensitivity profiles reveal that both divertors are less stable near the target compared to the X-point, particularly for the inner leg. This can inform the choice of the steady-state operational detachment front location and the associated diagnostics, which, like the strike point location, should be done in full consideration of relevant engineering constraints.

The results of this work show that accounting for the radiation distribution is very important to the assessment of advanced divertor configuration geometries with impurity seeding, even in high-power reactor-class devices. DLS-Extended provides a computationally affordable way to assess this early on in the divertor design process. The model can be used to quickly explore the leg geometry parameter space, allowing detachment performance to be optimised alongside engineering parameters in an equilibrium design workflow.

While there is a growing body of research investigating f_R and $L_{\parallel}$ effects in tokamaks, this work highlights the need for dedicated high-fidelity simulation and experimental magnetic geometry studies in seeded conditions.

Acknowledgments

The authors would like to thank Bruce Lipschultz for helpful discussions during this project.

This work was performed in part under the auspices of the U.S. Department of Energy by Lawrence Livermore National Laboratory under contract DE-AC52-07NA27344.

This project was funded by EPSRC CDT in the Science and Technology of Fusion Energy, Grants EP/L01663X/1, EP/S022430/1.

References

[1] Zohm H. Assessment of DEMO challenges in technology and physics. Fusion Engineering and Design. 2013;88(6-8):428-33.

[2] Loarte A, Lipschultz B, Kukushkin A, Matthews G, Stangeby P, Asakura N, et al. Power and particle control. Nuclear Fusion. 2007;47(6):S203.

[3] Kuang AQ, Ballinger S, Brunner D, Canik J, Creely AJ, Gray T, et al. Divertor heat flux challenge and mitigation in SPARC. Journal of Plasma Physics. 2020;86(5):865860505.

[4] Cowley C, Lipschultz B, Moulton D, Dudson B. Optimizing detachment control using the magnetic configuration of divertors. Nuclear Fusion. 2022 07;62(8):086046.

[5] Verhaegh K, Lipschultz B, Duval B, Harrison J, Reimerdes H, Theiler C, et al. Spectroscopic investigations of divertor detachment in TCV. Nuclear Materials and Energy. 2017;12:1112-7.

[6] Dudson BD, Allen J, Body T, Chapman B, Lau C, Townley L, et al. The role of particle, energy and momentum losses in 1D simulations of divertor detachment. Plasma Physics and Controlled Fusion. 2019;61(6):065008.

[7] Pshenov AA, Kukushkin AS, Krasheninnikov SI. Energy balance in plasma detachment. Nuclear Materials and Energy. 2017;12:948-52. Available from: `https://doi.org/10.1016/j.nme.2017.03.019`.

[8] Kallenbach A, Bernert M, Dux R, Casali L, Eich T, Giannone L, et al. Impurity seeding for tokamak power exhaust: From present devices via ITER to DEMO. Plasma Physics and Controlled Fusion. 2013;55.

[9] Lengyel L. Analysis of radiating plasma boundary layers. Max-Planck-Institut für Plasmaphysik; 1981.

[10] Moulton D, Stangeby PC, Bonnin X, Pitts RA. Comparison between SOLPS-4.3 and the Lengyel Model for ITER baseline neon-seeded plasmas. Nuclear Fusion. 2021 4;61.

[11] Järvinen AE, Aho-Mantila L, Lunt T, Subba F, Rubino G, Xiang L. Parametric scaling of power exhaust in EU-DEMO alternative divertor simulations. Nuclear Materials and Energy. 2023 3;34.

[12] Reinke ML. Heat flux mitigation by impurity seeding in high-field tokamaks. Nuclear Fusion. 2017;57.

[13] Lipschultz B, Parra FI, Hutchinson IH. Sensitivity of detachment extent to magnetic configuration and external parameters. Nuclear Fusion. 2016;56(5):056007.

[14] Myatra O, Lipschultz B, Moulton D, Verhaegh K, Dudson B, Orchard S, et al. Predictive SOLPS-ITER simulations to study the role of divertor magnetic geometry in detachment control in the MAST-U Super-X configuration. Nuclear Fusion. 2023 9;63.

[15] Theiler C, Lipschultz B, Harrison J, Labit B, Reimerdes H, Tsui C, et al. Results from recent detachment experiments in alternative divertor configurations on TCV. Nuclear Fusion. 2017 3;57.

[16] Reimerdes H, Duval BP, Harrison JR, Labit B, Lipschultz B, Lunt T, et al. TCV experiments towards the development of a plasma exhaust solution. Nuclear Fusion. 2017 9;57.

[17] Carpita M, Février O, Reimerdes H, Theiler C, Duval BP, Colandrea C, et al. Parallel flows as a key component to interpret Super-X divertor experiments. Nuclear Fusion. 2024 4;64.

[18] Maurizio R, Elmore S, Fedorczak N, Gallo A, Reimerdes H, Labit B, et al. Divertor power load studies for attached L-mode single-null plasmas in TCV. Nuclear Fusion. 2018 1;58.

[19] Covele B, Valanju P, Kotschenreuther M, Mahajan S. An exploration of advanced X-divertor scenarios

on ITER. Nuclear Fusion. 2014;54.

[20] Petrie TW, Canik JM, Lasnier CJ, Leonard AW, Mahdavi MA, Watkins JG, et al. Effect of changes in separatrix magnetic geometry on divertor behaviour in DIII-D. Nuclear Fusion. 2013 11;53.

[21] Brida D, Grenfell G, Grover O, Silvagni D, Faitsch M, Stroth U. Transport and profile broadening in the private flux region of ASDEX upgrade and role for power exhaust. Nuclear Fusion. 2025 2;65.

[22] Moulton D, Harrison JR, Xiang L, Ryan PJ, Kirk A, Verhaegh K, et al. Super-X and conventional divertor configurations in MAST-U ohmic L-mode; a comparison facilitated by interpretative modelling. Nuclear Fusion. 2024 7;64.

[23] Verhaegh K, Harrison J, Moulton D, Lipschultz B, Lonigro N, Osborne N, et al. Divertor shaping with neutral baffling as a solution to the tokamak power exhaust challenge. Communications Physics. 2025 12;8.

[24] Moulton D, Harrison J, Lipschultz B, Coster D. Using SOLPS to confirm the importance of total flux expansion in Super-X divertors. Plasma Physics and Controlled Fusion. 2017;59.

[25] Kallenbach A, Bernert M, Dux R, Reimold F, Wischmeier M. Analytical calculations for impurity seeded partially detached divertor conditions. Plasma Physics and Controlled Fusion. 2016;58.

[26] Gallo A, Fedorczak N, Elmore S, Maurizio R, Reimerdes H, Theiler C, et al. Impact of the plasma geometry on divertor power exhaust: Experimental evidence from TCV and simulations with SolEdge2D and TOKAM3X. Plasma Physics and Controlled Fusion. 2018 1;60.

[27] Meyer H. Plasma burn - Mind the gap. Philosophical Transactions of the Royal Society A: Mathematical, Physical and Engineering Sciences. 2024 8;382.

[28] Wiesen S, Reiter D, Kotov V, Baelmans M, Dekeyser W, Kukushkin AS, et al. The new SOLPS-ITER code package. Journal of Nuclear Materials. 2015;463:480-4. Available from: `http://dx.doi.org/10.1016/j.jnucmat.2014.10.012`.

[29] Osawa RT, Newton SL, Moulton D, Henderson SS, Badicel V, Hudoba A. Assessment of the impact of fuelling puff location on divertor impurity compression and enrichment in STEP. Nuclear Fusion. 2024 10;64.

[30] Cowley C. Modelling of Alternative Divertor Power Exhaust. University of York; 2024.

[31] FusionDLS Developers. FusionDLS: Detachment Location Sensitivity; 2025. Accessed: 2025-06-15. `https://github.com/FusionDLS/FusionDLS`.

[32] Henderson SS, Osawa RT, Newton SL, Moulton D, Xiang L, Futtersack R, et al. An overview of the STEP divertor design and the simple models driving the plasma exhaust scenario. Nuclear Fusion. Submitted:1337-48.

[33] Body T, Hasse C, cfsjamie. cfs-energy/radas: Zenodo release. Zenodo; 2024. Available from: `https://doi.org/10.5281/zenodo.14182360`.

[34] Body T, Kallenbach A, Eich T. A simple, accurate model for detachment access. Nuclear Fusion. 2025 8;65:086002. Available from: `https://iopscience.iop.org/article/10.1088/1741-4326/ade4d9`.

[35] Newton S, Osawa R, Henderson S, Moulton D, Myatra O, Badicel V. Enrichment of impurities seeded for exhaust control in a spherical tokamak power plant geometry. Nuclear Fusion. 2025;65(9):096026.

[36] Kotschenreuther M, Valanju P, Mahajan S, Zheng LJ, Pearlstein LD, Bulmer RH, et al. The super X divertor (SXD) and a compact fusion neutron source (CFNS). Nuclear Fusion. 2010;50.

[37] Fishpool G, Canik J, Cunningham G, Harrison J, Katramados I, Kirk A, et al. MAST-upgrade divertor facility and assessing performance of long-legged divertors. Journal of Nuclear Materials. 2013;438.

[38] Fil A, Lipschultz B, Moulton D, Dudson BD, Février O, Myatra O, et al. Separating the roles of magnetic topology and neutral trapping in modifying the detachment threshold for TCV. Plasma Physics and Controlled Fusion. 2020;62.

[39] Spitzer L, Härm R. Transport Phenomena in a Completely Ionized Gas. Physical Review. 1953 3;89:977-81. Available from: `https://link.aps.org/doi/10.1103/PhysRev.89.977`.

[40] Stangeby PC, et al. The plasma boundary of magnetic fusion devices. vol. 224. Institute of Physics Pub. Philadelphia, Pennsylvania; 2000.

[41] Goldston RJ, Reinke ML, Schwartz JA. A new scaling for divertor detachment. Plasma Physics and Controlled Fusion. 2017 3;59.

[42] Derks GL, Westerhof E, van Berkel M, Jenneskens JH, Koenders JTW, Mijin S, et al. Multi-machine benchmark of the self-consistent 1D scrape-off layer model DIV1D from stagnation point to target with SOLPS-ITER. Plasma Physics and Controlled Fusion. 2024 5;66.

[43] Kotschenreuther M, Valanju PM, Mahajan SM, Wiley JC. On heat loading, novel divertors, and fusion reactors. Physics of Plasmas. 2007;14.

[44] Raj H, Theiler C, Thornton A, Février O, Gorno S, Bagnato F, et al. Improved heat and particle flux mitigation in high core confinement, baffled, alternative divertor configurations in the TCV tokamak. Nuclear Fusion. 2022 12;62.

[45] Chen ZP, Kotschenreuther M, Mahajan S, Roeltgen J. SOLPS-ITER modeling of boosted carbon radiation through non-coronal effects in an X-divertor facilitating detachment in DIII-D. Nuclear Fusion. 2020;60.

[46] Hutchinson IH. Thermal front analysis of detached divertors and MARFEs. Nuclear Fusion. 1994;34:1337-48.

[47] Federici F, Reinke ML, Lipschultz B, Lovell JJ, Verhaegh K, Lonigro N, et al. Evolution of radiation profiles in a strongly baffled divertor on MAST Upgrade. Nuclear Materials and Energy. 2025 6;43:101940. Available from: `https://linkinghub.elsevier.com/retrieve/pii/S2352179125000821`.

[48] et al KHAV. The physics basis for implementing Alternative Divertor Configurations on reactors; 2025. Chengdu, China. Conference talk at the 30th IAEA Fusion Energy Conference.

[49] LaBombard B, Marmar E, Irby J, Terry JL, Vieira R, Wallace G, et al. ADX: A high field, high power density, advanced divertor and RF tokamak. Nuclear Fusion. 2015 5;55.

[50] Bernert M, Wiesen S, Février O, Kallenbach A, Koenders J, Sieglin B, et al. The X-Point radiating regime at ASDEX Upgrade and TCV. Nuclear Materials and Energy. 2023.

[51] Marinoni A, Sauter O, Coda S. A brief history of negative triangularity tokamak plasmas. Reviews of Modern Plasma Physics. 2021;5.

[52] Dudson B, Kryjak M, Muhammed H, Hill P, Omotani J. Hermes-3: Multi-component plasma simulations with BOUT++. Computer Physics Communications. 2024 3;296.

[53] Osawa RT, Moulton D, Cowley C, Henderson S, Hudoba A, Kryjak M, et al.. Assessment of detachment front movement in the divertor legs of STEP; 2022. Korea (virtual). Conference talk at the 25th International Conference on Plasma Surface Interaction in Controlled Fusion Devices.

[54] Fundamenski WR. Tokamak edge plasma modeling using an improved onion-skin method. University of Toronto; 1999.

[55] Virtanen P, Gommers R, Oliphant TE, Haberland M, Reddy T, Cournapeau D, et al. SciPy 1.0: Fundamental Algorithms for Scientific Computing in Python. Nature Methods. 2020;17:261-72.

[56] Carolan PG, Piotrowicz VA. The behaviour of impurities out of coronal equilibrium. Plasma Physics. 1983 10;25:1065-86. Available from: `https://iopscience.iop.org/article/10.1088/0032-1028/25/10/001`.

[57] Osawa RT, Moulton D, Newton SL, Henderson SS, Lipschultz B, Hudoba A. SOLPS-ITER analysis of a proposed STEP double null geometry: Impact of the degree of disconnection on power-sharing. Nuclear Fusion. 2023 7;63.

Appendix A. Numerical implementation

Like the original DLS model, the purpose of DLS-Extended is to obtain upstream conditions for a particular front location. Because of this, a front location s_f must be specified by the user, then the model integrates from this front to the upstream. In the analytical forms of

the DLS model, the front is defined as the location at which heat flux drops to zero. However, in the numerical version of the model, having T = 0, $q_{||} = 0$ at the start of integration means the temperature and heat flux profiles cannot evolve, as $\frac{dT}{ds} = \frac{dq_{||}}{ds} = 0$. The target heat flux is set to 5% of the upstream heat flux, which becomes the definition of the front location. The choice of value is arbitrary as long as it is close to zero; in this case 5% produced a closer match with SOLPS-ITER simulations.

The numerical solution of the two DLS-Extended equations (4 and 5) requires an iterative approach, as the equations are coupled through T_u which is a model output. In order to circumvent this, first the heat flux integral is estimated by assuming a heat flux which is constant above and linearly decreasing below the X-point:

$$\int_f^u q_\parallel ds_\parallel \approx q_{\parallel,u}(s_{\parallel,X} - s_{\parallel,f}) + \frac{1}{2} q_{\parallel,u} \frac{s_{\parallel,u} - s_{\parallel,X}}{s_{\parallel,u} - s_{\parallel,f}}. \tag{A.1}$$

This allows an estimate for the temperature:

$$T_{u,0} \approx \left(\frac{7}{2} \frac{\int_f^u q_\parallel ds_\parallel (s_{\parallel,u} - s_{\parallel,f})}{\kappa_{e,0}} \right)^{2/7}. \tag{A.2}$$

The solution algorithm nests two loops. The inner loop uses a simple gradient search method to find the value of the control variable C such that the heat flux is zero at the upstream midplane stagnation point and $q_\parallel$ rises towards the X-point according to the Q_{in} source. Once converged, the resulting T_u is fed back into the calculation as $T_{u,0}$ and the inner loop is repeated. This procedure comprises the outer loop which continues until $T_u^{i+1} - T_u^i$ drops below another user set tolerance (0.001 by default). This algorithm was inspired by the work in [12]. The model is written entirely in Python and takes approx. 1-2 seconds per solution, as compared to the near-instant analytical form of the original DLS. The integration is done using the solve_ivp ODE solver in Python's SciPy package [55].

Appendix B. Detailed comparison to SOLPS-ITER

Appendix B.1. Cooling curve selection

In the SOLPS simulation, the transport and radiative properties of individual argon charge states are fully simulated. In DLS-Extended, the fixed-fraction model is used: the impurity is a fixed fraction of the local electron density and the radiation is calculated as a function of temperature using an impurity radiation cooling curve. The curve is calculated using the open-source tool radas [33] based on OpenADAS data. This requires the assumption of a constant background electron density and impurity residence time, together referred to as the $n_e\tau$ parameter [56]. Figure B1 shows a selection of constant $n_e\tau$ curves compared to curves extracted from SOLPS using equation 17.

It can be seen that there is considerable variation between the SOL rings, in particular for the outer leg. The SOLPS curves have distinct features - the sharp cut-off at the high

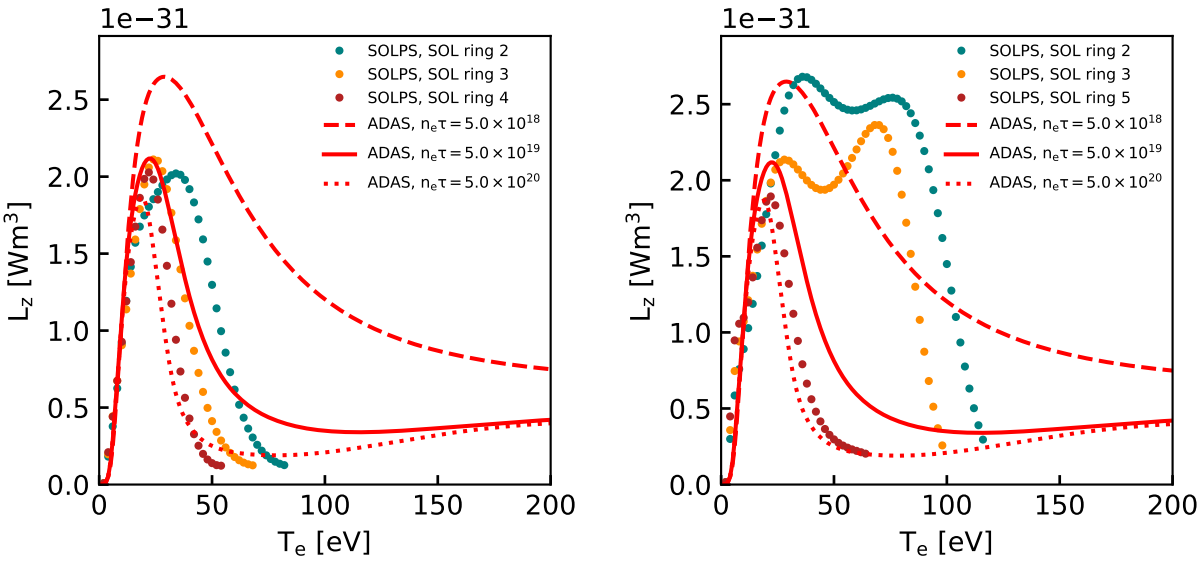

(a) Inner divertor

(b) Outer divertor

Figure B1: Comparison of cooling curves extracted from SOLPS for each SOL ring (dots) to selected constant $n_e\tau$ curves (lines) for the inner and outer divertor. Each SOL ring has a different curve, and none can be captured by a constant $n_e\tau$ in the high temperature region. The $n_e\tau = 5 \times 10^{19}\mathrm{m}^{-3}\mathrm{ms}$ curve is selected based on an ITER study [10] as a plausible choice if no high-fidelity simulation was available.

temperature end (due to lack of data at high temperatures in the simulation) and the double peak in some outer SOL rings (of unknown origin). There is also a steady decline towards the temperature cut-off, similar to that seen in [10]. It was found that no constant $n_e\tau$ curve can reproduce these features, which additionally vary between SOL rings. While considerably more effort could be spent on selecting an appropriate $n_e\tau$ parameter on a SOL ring basis (including using the simple model introduced in [22]), the entire assumption of a constant $n_e\tau$ is questionable and users of simple models cannot always rely on the availability of high fidelity simulations. Therefore, we select a value from [10], which represents a plausible choice if no high fidelity simulation data is available. The value of $n_e\tau = 5 \times 10^{19}\mathrm{m}^{-3}\mathrm{ms}$ was originally found for ITER and offers some approximation of the real curve in each divertor. We let the discrepancy in the results be an indication of the sensitivity to cooling curve choice.

Appendix B.2. Results

Section 3 showed the comparison of the radiation distribution prediction for SOL ring 3. In this section, two additional SOL rings are selected for each divertor. In the outer, we add ring 2 which is affected by a nearby argon puff, and ring 5 where convective heat transfer plays a large role. For the inner, we add rings 2 and 4 which feature different degrees of

convective heat flux strength. As in section 3, there are three DLS-Extended results sets: using the constant $n_e\tau = 5 \times 10^{19}\mathrm{m}^{-3}\mathrm{ms}^{-1}$ curve, switching to the argon curve extracted from SOLPS, and finally, using the SOLPS curve alongside a tuned conductivity to improve the radiation distribution match. The purpose of the constant $n_e\tau$ curve is to show the impact of not having access to high-fidelity simulations and having to rely on literature for the $n_e\tau$ parameter, with the value obtained from an ITER study [10]. The conductivity tuning allows the radiation distribution to be matched near-exactly for the purposes of strike point optimisation.

Figure B2 shows a detailed comparison of the three outer divertor rings to SOLPS, with rings 2, 3 and 5 shown in the top, middle and bottom row, and the columns corresponding to different comparison parameters. The first column shows the cumulative radiation integral fraction, the second electron temperature and the third and fourth columns show argon and electron density, respectively. Since the model is set up for the density and power to be inputs and the impurity fraction as the output, the argon density profiles can change between DLS-Extended simulations. The final column shows parallel electron conductive heat flux as a fraction of the total parallel heat flux, with DLS-Extended assuming a fraction of 1.

The first major observation is that all three rings feature non-negligible radiation above the X-point, and so can be considered "broadly radiating". SOL ring 2 is particularly broad, having only dissipated 25% power in the first 10m above the target. This phenomenon also occurs in ring 1 (not shown). It is likely caused by the argon puff located nearby on the divertor chamber floor on the PFR side (see figure 1 in [29]), which manifests as a peak in electron and argon density around the 10m mark. This significantly increases local radiation, resulting in a near-total dissipation of the conductive electron heat flux. The subsequent reduction in both densities rapidly reduces radiative power, leading to a plateau in cumulative radiation. This effect is not captured by DLS-Extended due to the assumption of pressure conservation and fixed impurity density fraction, leading to a significant under-prediction of radiation width. The other SOL rings, 3 and 5, show much weaker density variation which results in smoother cumulative radiation profiles.

The second major finding is that the prediction of upstream temperature and even the temperature profile is remarkably good even without tuning, despite the constant conductivity and lack of convective heat transfer in DLS-Extended. This result is likely because it is the conduction that dominates the temperature gradient, as well as that T_u has only a weak 2/7 dependence on the conductivity.

Finally, it is clear that using the exact cooling curve leads to better results. SOL rings 2 and 3 feature a double peak absent from the constant $n_e\tau$ curves (see figure B1b). The additional peak increases radiation at high temperatures, broadening radiation compared to a constant $n_e\tau$.

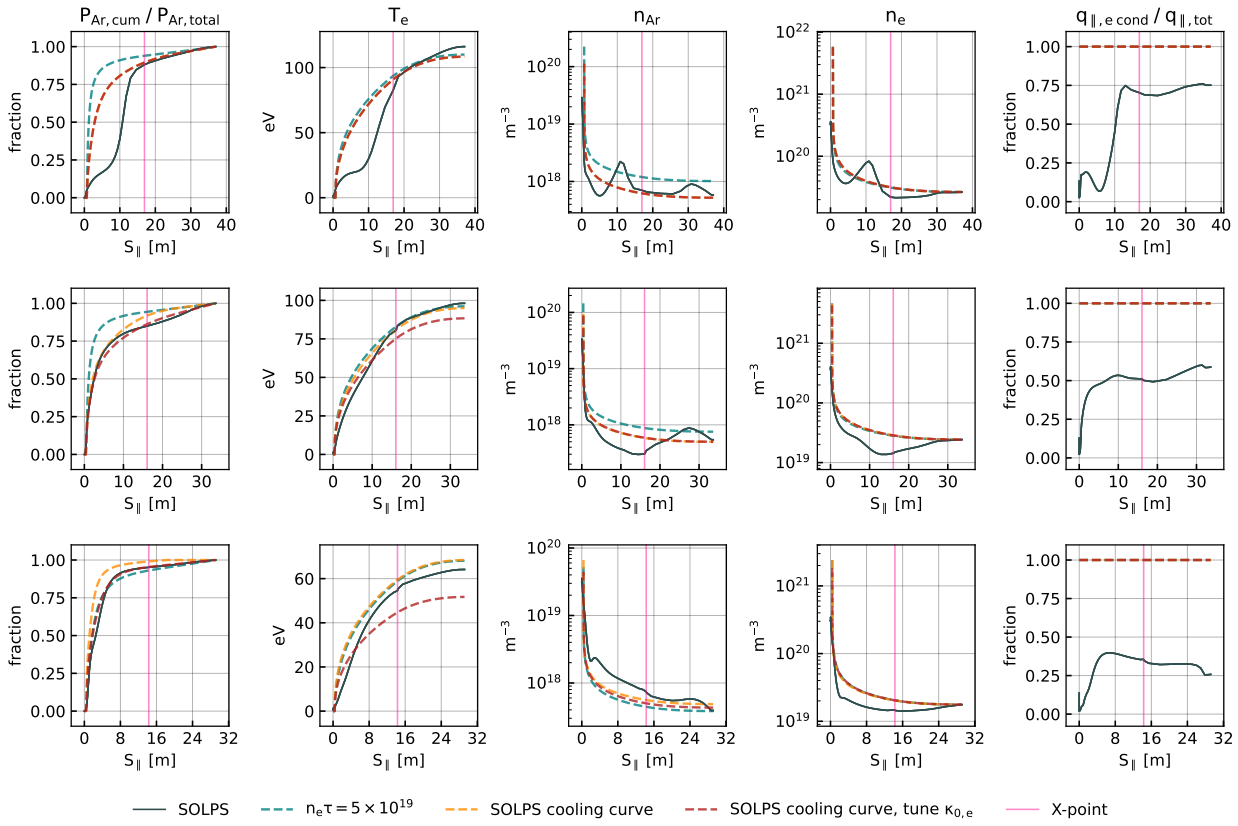

Figure B2: Comparison of DLS-Extended profiles to SOLPS results for the outer divertor. SOL rings 2, 3 and 5 are shown in the top, middle and bottom row, respectively. The columns in order from left to right: normalised cumulative argon radiation integral, electron temperature, argon density, electron density and electron conductive heat flux as a ratio of total parallel heat flux.

The process is repeated for the inner divertor with results shown in figure B3. Once again, SOLPS shows that argon radiation is broad and extends throughout the entire divertor region. The results are more sensitive to the puff locations than in the outer divertor; the inboard midplane fuelling puff is closer to the separatrix (see figure 1 in [57]) and leads to significant convective flows upstream. This is shown in the results as a peak in electron density at the midplane as well as a reduction in electron temperature and a dramatic reduction in electron conduction due to the shallower, and even inverted, temperature gradient. The argon puff is located in line with the X-point and results in a local peak in argon density. None of these effects can be captured in DLS-Extended, and the match suffers - particularly in the upstream electron temperature.

The influence of choosing the exact cooling curve is significant because the constant $n_e\tau$ cooling curve features more high-temperature radiation compared to the SOLPS curves which are cut off at the upstream temperature. This allows more radiation at the higher

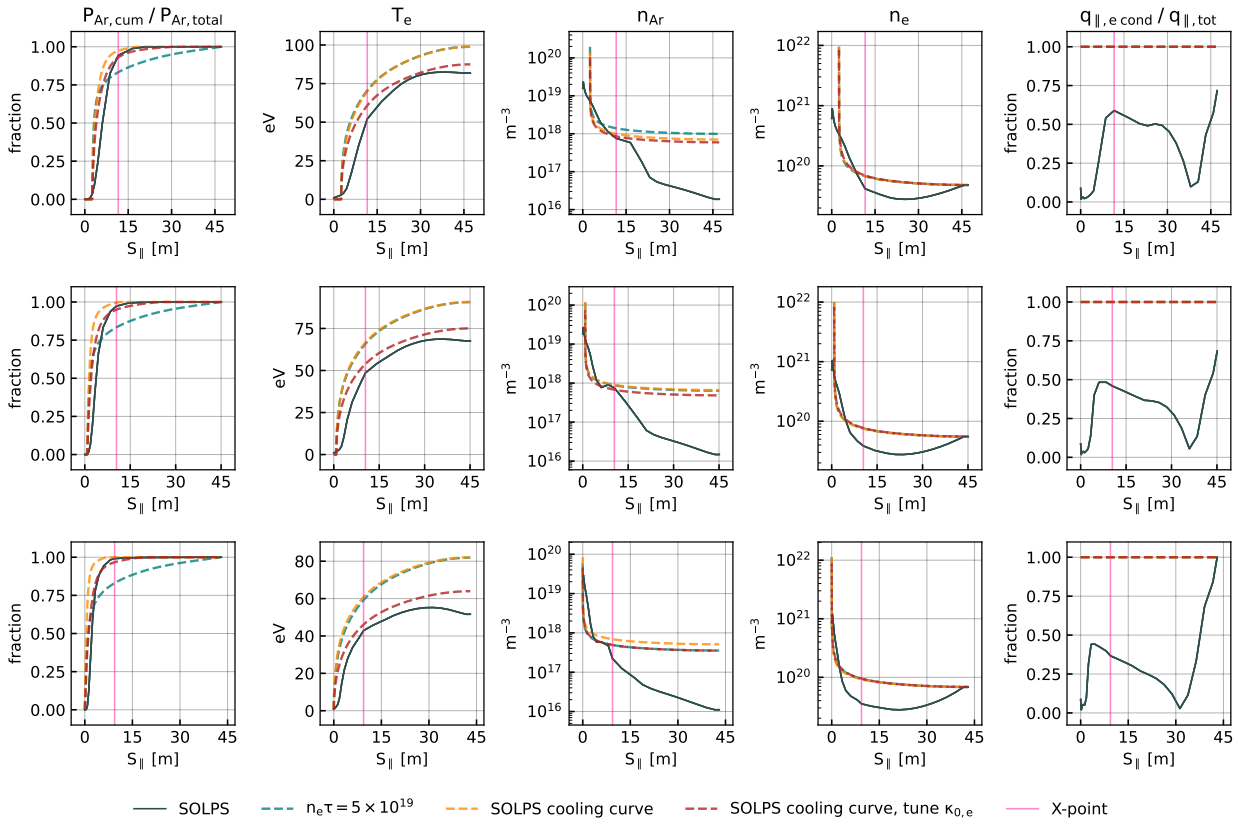

Figure B3: Comparison of DLS-Extended profiles to SOLPS results for the inner divertor, with SOL rings 2, 3 and 4 shown in the top, middle and bottom row, respectively. The columns are the same as figure B2.

temperatures seen in DLS-Extended, broadening the radiation distribution. It's a more pronounced difference than for the outer, because the outer SOLPS cooling curves feature a lot of upstream radiation thanks to their yet unexplained double peak feature (see figure B1.

DLS-Extended attains a surprisingly good match in impurity radiation distribution when the exact cooling curve is used, especially considering the differences in the temperature and density profiles - this is because these differences are mostly located above the X-point, where there is less radiation. The remaining disagreement is due to SOLPS featuring lower temperatures immediately downstream of the X-point, allowing more radiation there and broadening the distribution. This is evidenced by the fact that when the conductivity is tuned to better match the radiation distribution, the temperature profile match is significantly improved.

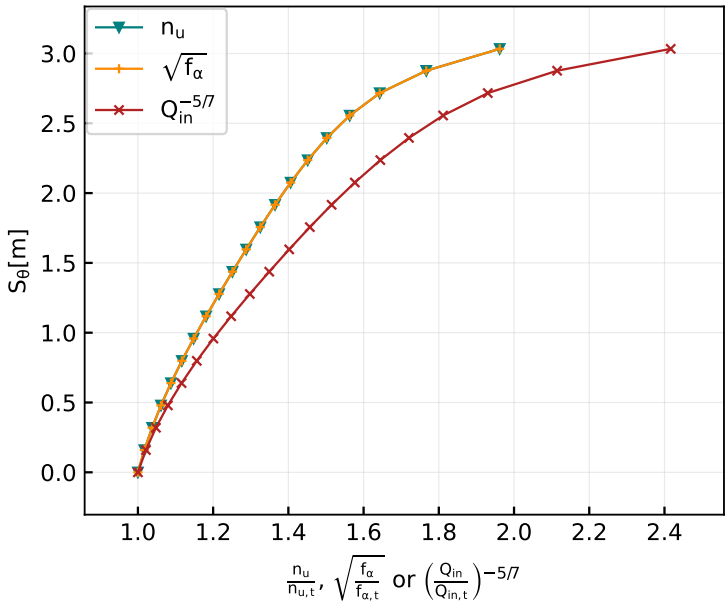

Figure C1: Front location scan using density, impurity fraction and power as evolved variables, shown as the evolution of each actuator with the poloidal front position. The actuator value has been scaled according to the control variable definition from the original DLS model (7) and normalised to the value at detachment threshold.

Appendix C. Impact of using power as control variable

Unlike in the original DLS model, the DLS-Extended does not allow for density, impurity fraction and power to be used interchangeably with an appropriate scaling. This is because unlike density and impurity fraction, changing the power has an additional effect of changing the radiation distribution: greater power steepens the temperature gradient, shrinking the size of the radiation region.

To show the magnitude of this effect, a scan in front position was performed for the outer divertor baseline from section 3 using each of the three actuators. The results are shown in figure C1. While density and impurity fraction are still interchangeable, actuating the front using the power source changes the result, increasing the detachment window by approx. 20% and reducing local sensitivity. This is because as the front moves upstream due to the reducing power, the radiation region becomes broader, changing the impact of the radiation-driven effects. A detailed investigation into this mechanism is left for future work.

Appendix D. Detachment effects derivation

In this section, we present the derivation of equation 13 which is used to break down the radiation distribution effects in section 6.1.

$$B\frac{d}{ds}\left(\frac{q_{||}}{B}\right) = n^2 f_\alpha L_\alpha(T) - Q_{radial}. \tag{D.1}$$

By multiplying the equation by $\frac{2}{B^2}$, and using the chain rule, Equation D.1 can be written:

$$\frac{d}{ds}\left(\frac{q_{||}^2}{B^2}\right) = 2\frac{q_{||}}{B}\frac{d}{ds}\left(\frac{q_{||}}{B}\right) = \frac{2q_{||}n^2 f_\alpha L_\alpha(T)}{B^2} - \frac{2q_{||}Q_{radial}}{B^2}. \tag{D.2}$$

This may be integrated from the X-point, denoted by subscript X, to the leading edge of the detachment front, denoted by subscript f:

$$\frac{q_{||,X}^2}{B_X^2} - \frac{q_{||,f}^2}{B_f^2} = \int_{s=0}^{s=L_{||}} \frac{2q_{||}n^2 f_\alpha L_\alpha(T)}{B^2} ds - \int_{s=0}^{s=L_{||}} \frac{2q_{||}Q_{radial}}{B^2} ds. \tag{D.3}$$

In the context of this simple model, the detachment front is the region where all of the heat flux is dissipated by impurity radiation, and as a result the heat flux at the downstream end of this front disappears. At the midplane, the heat flux is also 0, hence the LHS of the equation disappears:

$$\int_{s=s_X}^{s=L_{||}} \frac{2q_{||}Q_{radial}}{B^2} ds = \int_{s_{f,||}}^{L_{||}} \frac{2q_{||}n^2 f_\alpha L_\alpha(T)}{B^2} ds. \tag{D.4}$$

Keep in mind the integration range from the radial heat source is shortened to only consider the upstream, because Q_{radial}=0 upstream of the X-point. Next, it is assumed that the electron static pressure above the downstream end of the front remains constant, such that density can be expressed: $n = \frac{n_u T_u}{T}$. The resulting equation is:

$$2Q_{radial}\int_{s=s_X}^{s=L_{||}} \frac{q_{||}}{B^2} ds = 2f_\alpha n_u^2 T_u^2 \int_{s_{f,||}}^{L_{||}} \frac{q_{||}L_\alpha(T)}{T^2 B^2} ds. \tag{D.5}$$

Then, the heat flux is assumed to be entirely electron conducted, such that $q_{||}$ can be replaced with $\kappa_{e0}T^{5/2}\frac{dT}{ds}$:

$$2Q_{radial}\int_{s=s_X}^{s=L_{||}} \frac{q_{||}}{B^2} ds = 2f_\alpha n_u^2 T_u^2 \int_{s_{f,||}}^{L_{||}} \frac{\kappa_{e0}T^{1/2}L_\alpha(T)}{B^2} dT. \tag{D.6}$$

or:

$$\sqrt{2Q_{radial}\int_{s=s_X}^{s=L_{||}} \frac{q_{||}}{B^2} ds} = \sqrt{f_\alpha} n_u T_u \sqrt{2\int_{s_{f,||}}^{L_{||}} \frac{\kappa_{e0}T^{1/2}L_\alpha(T)}{B^2} dT}. \tag{D.7}$$

Or:

$$\sqrt{f_\alpha} n_u = \frac{1}{T_u} \frac{\sqrt{2Q_{radial}\int_{s=s_X}^{s=L_{||}} \frac{q_{||}}{B^2} ds}}{\sqrt{2\int_{s_{f,||}}^{L_{||}} \frac{\kappa_{e0}T^{1/2}L_\alpha(T)}{B^2} dT}}. \tag{D.8}$$

Now we will do something strange. It will make sense later, when we consider the simple DLS model. In certain terms that depend on heat flux let us divide by the radial heat source:

$$\sqrt{f_\alpha} n_u = Q_{radial}^{-2/7} \frac{Q_{radial}^{2/7}}{T_u} \frac{\sqrt{2 Q_{radial}^2 \int_{s=s_X}^{s=L_{||}} \frac{q_{||}}{Q_{radial} B^2} ds}}{\sqrt{2 \int_{s_{f,||}}^{L_{||}} \frac{\kappa_{e0} T^{1/2} L_\alpha(T)}{B^2} dT}}. \tag{D.9}$$

Or:

$$\frac{\sqrt{f_\alpha} n_u}{Q_{radial}^{5/7}} = \frac{Q_{radial}^{2/7}}{T_u} \frac{\sqrt{2 \int_{s=s_X}^{s=L_{||}} \frac{q_{||}}{Q_{radial} B^2} ds}}{\sqrt{2 \int_{s_{f,||}}^{L_{||}} \frac{\kappa_{e0} T^{1/2} L_\alpha(T)}{B^2} dT}}. \tag{D.10}$$

Let us now rewrite:

$$\frac{1}{\sqrt{2 \int_{s_{f,||}}^{L_{||}} \frac{\kappa_{e0} T^{1/2} L_\alpha(T)}{B^2} dT}} = B_{eff} \frac{1}{\sqrt{2 \int_{s_{f,||}}^{L_{||}} \kappa_{e0} T^{1/2} L_\alpha(T) dT}} \tag{D.11}$$

where:

$$B_{eff} = \frac{\sqrt{2 \int_{s_{f,||}}^{L_{||}} \kappa_{e0} T^{1/2} L_\alpha(T) dT}}{\sqrt{2 \int_{s_{f,||}}^{L_{||}} \frac{\kappa_{e0} T^{1/2} L_\alpha(T)}{B^2} dT}} \tag{D.12}$$

Such that the DLS equation becomes:

$$\frac{\sqrt{f_\alpha} n_u}{Q_{radial}^{5/7}} = B_{eff} \frac{Q_{radial}^{2/7}}{T_u} \frac{\sqrt{2 \int_{s=s_X}^{s=L_{||}} \frac{q_{||}}{Q_{radial} B^2} ds}}{\sqrt{2 \int_{s_{f,||}}^{L_{||}} \kappa_{e0} T^{1/2} L_\alpha(T) dT}}. \tag{D.13}$$

It is straightforward (yet tedious) to show that in the limit of the simple DLS model, the term B_{eff} becomes the front magnetic field, the extended DLS upstream temperature reduces to the simple DLS temperature, and the final term remains constant.